Surface Forces Apparatus measurements of interactions between rough and reactive calcite surfaces

Joanna Dziadkowiec*[,a], Shaghayegh Javadi[a,b,c], Jon E. Bratvold[d], Ola Nilsen[d], Anja Røyne[a]

[a] Physics of Geological Processes (PGP) , The NJORD Centre, Department of Physics, University of Oslo, Norway

[b] The National IOR center of Norway, University of Stavanger, Norway.

[c] Petroleum engineering department, University of Stavanger, Norway.

[d] Centre for Materials Science and Nanotechnology (SMN), Department of Chemistry, University of Oslo, Norway

KEYWORDS: Surface Forces Apparatus, calcite, force measurements, rough surfaces, calcite polycrystalline films, water-weakening, confinement

ABSTRACT

Nm-range forces acting between calcite surfaces in water affect macroscopic properties of carbonate rocks and calcite-based granular materials, and are significantly influenced by calcite surface recrystallization. We suggest that the repulsive mechanical effects related to nm-scale surface recrystallization of calcite in water could be partially responsible for the observed decrease of cohesion in calcitic rocks saturated with water. Using the Surface Forces Apparatus (SFA), we simultaneously followed the calcite reactivity and measured the forces in water in two surface configurations: between two rough calcite surfaces (CC), or between rough calcite and a smooth mica surface (CM). We used nm-scale rough, polycrystalline calcite films prepared by Atomic Layer Deposition (ALD). We measured only repulsive forces in CC in $CaCO_3$-saturated water, which was related to roughness and possibly to repulsive hydration effects. Adhesive or repulsive forces were measured in CM in $CaCO_3$-saturated water depending on calcite roughness, and the adhesion was likely enhanced by electrostatic effects. The pull-off adhesive force in CM became stronger with time and this increase was correlated with a decrease of roughness at contacts, which parameter could be estimated from the measured force-distance curves. That suggested a progressive increase of real contact areas between the surfaces, caused by gradual pressure-driven deformation of calcite surface asperities during repeated loading-unloading cycles. Reactivity of calcite was affected by mass transport across nm to µm-thick gaps between the surfaces. Major roughening was observed only for the smoothest calcite films, where gaps between two opposing surfaces were nm-thick over µm-sized areas, and led to force of crystallization that could overcome confining pressures of the order of MPa. Any substantial roughening of calcite caused a significant increase of the repulsive mechanical force contribution.

Introduction

Calcite is a crucial rock-forming, cement-forming and accessory mineral, significant in biomineralization and in the global CO_2 cycle. Nanometer-range, repulsive or attractive forces, acting between calcite surfaces in aqueous solutions, are critical to overall mechanical strength of calcite-bearing rocks [1-2], biomineralization processes, enhanced oil recovery (EOR) in chalk [3], and a range of industrial materials, in which granular calcite is used as an excipient, filler or a principal ingredient [4-7].

Forces between surfaces are severely affected by the properties of the surrounding liquid medium, and for calcite these interactions are further complicated by its reactivity and roughening on exposure to water. This has major implications both for colloidal systems and for rocks that undergo water-induced weakening. The water weakening phenomenon is related to a substantial loss of mechanical strength in fluid-saturated rocks. Diffusion of reactive fluids into solid-solid contacts in rocks amplifies subcritical crack growth, pressure solution and compaction, and thus contributes to a long-term creep deformation [8]. Water weakening is found to be most severe in porous, sedimentary rocks, including carbonates [9]. Although substantial compaction in chalk reservoirs, induced by water injection [10], has been studied in-depth, the lingering question remains about the dominant mechanism causing the observed subsidence. Risnes, et al. [2] used mixtures of water and ethylene glycol to show that chalk strength decreases with increasing water activity of the pore fluid, and attributed the observed loss of cohesion mainly to repulsive forces due to water adsorption on calcite surfaces. Although many other mechanisms apart from the hydration forces have been associated with the water weakening in carbonates [11-19], there has been no prior study to link this phenomenon with the reactivity and nm-scale surface roughening of calcite in water.

Despite the presence of repulsive forces between calcite surfaces in aqueous solutions in many systems [2, 17, 20-22], the very nature of this interaction is only beginning to be understood. In recent experiments, nm-ranged forces between two calcite surfaces [23] or calcite-silica surfaces [24] have been

directly measured by Atomic Force Microscopy (AFM). In contrast to the adhesive interaction between freshly cleaved calcite surfaces in air and in ethylene glycol, Røyne, et al. [23] reported strong repulsive forces when the medium between the surfaces was $CaCO_3$-presaturated water. The magnitude of this force significantly exceeded the theoretical DLVO electric double layer repulsion [25], and was attributed to the hydration forces acting between the highly hydrophilic calcite surfaces. Such hydration repulsion was further resolved by Diao and Espinosa-Marzal [24] who evidenced the oscillatory nature of this force, a phenomenon related to the layering of water populated by counterions in different hydration states. These findings indicate that the nature of repulsive forces between calcite surfaces is related to the already well-established molecular details of a calcite-solution interface [26-29].

Surface roughness remains insufficiently addressed in the complex interactions between calcite surfaces. Water wettability of calcite surface has been found to increase with its roughness [30]. This observation was further emphasized by Chen, et al. [31] for EOR systems, in which dilute electrolyte solutions enhance oil desorption from calcite surfaces both by affecting colloidal forces and by increasing calcite surface roughness. It has been shown that even nanoscale details of surface topography can affect the forces acting between mineral surfaces [25, 32]. Roughness not only decreases the contact area between the surfaces, but also disturbs the arrangement of surface species, and generates a repulsive force due to elastic deformation of the highest asperities [33-34]. Moreover, calcite surfaces display strong, local variations of surface charge related to details of surface topography, as predicted by recent modelling studies [35]. Changes in roughness may thus severely affect forces between calcite surfaces, which are reactive and dynamic in contact with aqueous solutions [36]. Additionally, although varied in magnitude and range, both hydration forces and roughness often add an exponentially repulsive component to the total force acting between the surfaces, which complicates the interpretation of the measured forces [23, 33]. Here, we investigate the effect of surface roughness and calcite reactivity on forces between calcite surfaces by employing polycrystalline calcite substrates with multiple asperity contacts.

Even though AFM is an extremely powerful tool in force measurements, it usually provides no information about the instantaneous changes in contact surface topography. In this work, we used the Surface Forces Apparatus (SFA), a unique force measuring technique that enables real time, *in situ* observations of surface alteration processes by multiple beam interferometry (MBI) [31, 37-38]. Unlike AFM, the SFA enables to study dynamic processes at an interface between two macroscopic surfaces with nm- to µm-scale resolution. The SFA geometry induces confinement conditions, where nm-thick liquid films can be trapped between the surfaces, and makes such measurements relevant for interfacial regions in rocks and materials. We thus can follow how the nm- to µm-scale growth, dissolution and related changes in surface roughness in µm-sized contact areas affect the magnitude and range of forces between dynamic and rough, polycrystalline calcite surfaces. Moreover, we present a feasible setup for measuring interactions between calcite surfaces in the SFA, which technique is becoming more frequently used to study forces between various mineral surfaces [31, 39-43] .

Materials and Methods

Preparation of Calcite Films

Thin, polycrystalline films of calcite were grown by the atomic layer deposition (ALD) method using a commercial F-120 Sat reactor from ASM Microchemistry. The process was adapted from Nilsen, et al. [44] with $Ca(thd)_2$ (Volatec; 97 %; Hthds = 2,2,6,6-tetramethylheptan-3,5-dione) and ozone as reaction precursors. To ensure deposition of phase-pure and crystalline $CaCO_3$, CO_2 (Praxair; 99.7 % pure) was pulsed after O_3, in line with the findings of Nilsen, et al. [44]. A constant carrier gas flow was provided from bottled N_2 (Praxair; 99.999 %). $Ca(thd)_2$ was kept at 195 °C to ensure sufficient sublimation, and ozone was generated by feeding O_2 (Praxair; 99.5 %) into an ozone generator (In USA AC series) producing ca. 15 % (200 g/N·m^3) O_3 at a flow of ca. 500 sccm. The deposition temperatures ranged from 250 to 350 °C. Thicknesses and refractive index values (at λ = 632.8 nm) were investigated using a spectroscopic ellipsometer (J. A. Woollam alpha-SE), fitting the data to a Cauchy model (CompleteEASE) for transparent films. Additional modelling was performed using the SFA in Reflcalc software [45] (Supplementary Information; **SI, S1)**. Film thickness varied between 100 and 200 nm, depending on the number of deposition cycles (detailed parameters in **SI, S3**).

Preparation of SFA Samples

SFA measurements require µm sample thickness and a semi-reflective metal layer present on back side of samples. Thus, ALD calcite films were deposited on mica substrates **(Figure 1A)**. The mica substrates were first freshly cleaved into uniformly thick (1–10 µm) layers [46], placed on a freshly-cleaved mica backing sheet, and coated with a 45 nm-thick layer of Au (with E-beam Leybold L560 evaporator). Subsequently, these Au-coated pieces of mica were flipped over to expose the Au-free surface, and were placed on a freshly cleaved mica backing sheet (15 x 5 cm^2) with the Au surface facing down. To avoid any glue or tape in the ALD reaction chamber, the pieces of Au-mica were clamped down on each end with stripes of freshly cleaved mica, which adhered to the mica backing plate. The use of standard Ag-coated mica or mica that was pre-attached on SFA disks with epoxy glue was not feasible due to oxidation of Ag

or epoxy decomposition inside the ALD chamber at temperatures reaching up to 350 °C. The Au-free mica surface was exposed to air just before the deposition of the calcite films, and the sample was handled in a laminar flow cabinet at all times. After calcite deposition the obtained calcite/mica/Au films were glued with EPON 1004F to standard SFA cylindrical disks (SurForce LLC; R = 0.02 m). Alternatively, calcite films were deposited on SFA glass disks **(Figure 1B)** or flat glass slides for characterization, both previously coated with 4 nm thick Ti and 45 nm thick Au layers. Ti was used to improve adhesion of Au to glass. The initial rms roughness of Ti/Au layer on glass was 0.8 nm (AFM scan size 5x5 μm^2). Calcite films deposited on the Au-coated SFA disks were not used in symmetric systems (calcite-calcite), due to insufficient thickness of calcite layer, and were only used in mica-calcite experiments. For these, bare mica surfaces were prepared [46]: pieces of freshly cleaved, optical-grade, 1–10 µm-thick mica sheets (S&J Trading Inc., USA), were cut using a hot platinum wire under laminar flow, and back-silvered (55 nm) with a thermal evaporator (Balzers BAE 250).

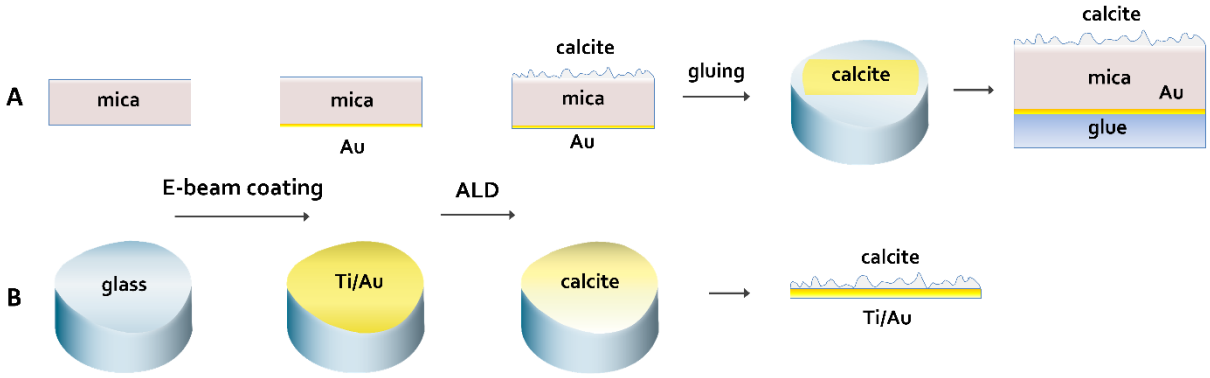

Figure 1. *Scheme showing two routes of calcite films preparation for SFA measurements on standard cylindrical SFA disks with the radius of curvature R = 0.02 m. E-beam coating was used to deposit metal layers (Au – gold and Ti – titanium); ALD was used to deposit calcite layers. A. calcite deposited on mica substrate; B. calcite deposited on Au-coated glass disks.*

SFA Measurements

Force measurements were performed with the Surface Forces Apparatus (SFA2000; SurForce LLC, USA [47]), equipped with a spectrometer (Princeton Instruments IsoPlane SCT320 with a PIXIS2048B camera)

for MBI, and a camera (Thorlabs DCC1645C) for surface topography observations (resolution of 0.015 µm/pixel). The SFA technique has been described in detail elsewhere [47-51]. The SFA spring constant (k = $2 \cdot 10^3$ N/m) was calibrated by applying known weights to the SFA spring and measuring the displacements. Measured forces were normalized with the local radius of curvature R of surfaces **(Figure S9)** through the Derjaguin approximation [52]. The SFA spectrometer was calibrated in the wavelength (λ) range 520–630 nm, using a Hg light source (Princeton Instruments, Intellical). Spectrometer gratings with different resolutions and a λ range (600, 1200 or 1800 g/mm) were used depending on sample thickness. Reference images of two surfaces in contact were captured using the 'step and glue' mode, in the full λ range 520–630 nm **(SI, S1.6)**. SFA data was analyzed by simulating the FECO fringe patterns using the open source Reflcalc software [45], which uses the matrix method for stratified samples adapted from Schubert [53]. Wavelength positions of FECO fringes were identified using MATLAB software **(SI, S1)**. SFA enables to observe changes in surface topography *in situ*, which are indicated by a shape of the FECO fringes [37] (here with a lateral resolution of 0.624 µm/pixel). Large contact areas (radius of 50–150 µm) in SFA allow to study influence of confinement on surface recrystallization, where nm-thick liquid films are trapped between the contacting surfaces over µm-sized areas.

Characterization of Calcite Films

AFM was used to measure topography of ALD films. We used a JPK NanoWizard®4 Bioscience AFM, in QI-mode, with a ContAl-G cantilever (NanoSensors, k = 0.2 N/m and l = 450 µm). Initial roughness of surfaces was analyzed in air, within maximum 2 weeks after each deposition (samples were stored in a desiccator cabinet). Several samples were used to follow the evolution of roughness for up to 3 hours in $CaCO_3$-saturated solutions in a ~3.5 ml fluid cell, semi-sealed with a silicon ring (under stationary fluid conditions, with no fluid exchange). The final topography of the samples used for the SFA experiments was measured after drying them gently with N_2 or in air. The AFM was kept in a temperature-controlled enclosure, at 24.5 ±0.5 °C. Scan size varied between 0.5x0.5 and 60x60 µm^2 to account for variation in size

and density of asperities, and the samples were scanned in several positions. Surface roughness data was characterized by root mean square (rms) values of the height data, calculated as $rms = \sqrt{\frac{1}{N}\sum_{i=1}^{N} y_i^2}$, where *N* is the number of height data points and *y* is the measured height in each point.

Raman spectra were collected using a Jobyn–Yvon Horiba T64000 instrument in the wavenumber range between 843 and 1338 cm^{-1}, using the laser operating at 787 nm, and with the spectral resolution of 2.0 cm^{-1} (grating 900 lines/mm). For each measurement, five scans of 120 s were averaged, and background fluorescence was corrected by fitting polynomial functions. The spectra were calibrated using two peaks of the paracetamol standard at 857.9 cm^{-1} and 1323.9 cm^{-1}.

X-ray diffraction (XRD) analysis was performed on calcite films deposited on Au-coated glass slides, with a Bruker AXS D8 Discover powder diffractometer in Bragg-Brentano configuration, equipped with a Lynxeye detector, using Cu Kα1 radiation and a Ge(111) monochromator.

Scanning Electron Microscopy (SEM) was performed using Hitachi SU5000 FE-SEM to observe the initial and final morphology of samples, which were gently dried with N_2, immediately after the SFA experiments. The samples were coated with Au, and images were collected using secondary electrons (SE) at accelerating voltage of 10 kV or 15 kV.

Solutions

$CaCO_3$-saturated solutions used in the SFA and AFM were prepared by presaturating deionized water (Milli-Q, 18.2 MΩ) for a week or more with an excess amount (~1 g/L) of synthetic, ultrapure calcite powder (Merck KGaA), which was baked at 300 °C for 2 hours, prior to use. All solutions were filtered with 0.45 µm polyether-sulfone Macherey-Nagel syringe filters, prior to use in the SFA. pH of the solutions was measured with the S470 SevenExcellence™ Toledo Mettler instrument. Ca^{2+} concentration was measured by AAS (Perkin Elmer AAnalyst 400 Atomic Absorption Spectrometer), with 0.4 ml of 10% $LaCl_3$ per 4 ml of a water sample ($LaCl_3 \cdot H_2O$, Prolabo Rectapure®, 99.99%) used as a Ca^{2+} release agent. Calcite saturation index (SI) was calculated with PHREEQC (phreeqc database) using the AAS-measured Ca^{2+} concentration

and measured pH values, assuming atmospheric CO_2 partial pressure of $pCO_2 = 3.5$ ($10^{-3.5}$ atm) for open systems and $pCO_2 = 10^{-6.2}$ atm for closed systems. Each time a solution was injected into the SFA chamber, it was rinsed with excess amount (~150 ml) of the injected solution to reduce any possible contamination. Solutions were usually injected with two surfaces brought into close contact, to limit their fast dissolution upon equilibration.

Results and Discussion

Characterization of Calcite Films

SEM images indicated that polycrystalline calcite films were initially composed of triangular, nm-sized (<50 nm) crystals, the morphology of which could not be precisely resolved with SEM. The films were continuous over cm-sized areas, with the presence of bigger, µm-sized, polycrystalline aggregates on some of the surfaces **(Figure 2A, B)**. These aggregates were composed of overgrown crystals with a rhombohedral morphology characteristic for calcite, with dominant {104} bounding faces. The aggregates were present in varied amounts for each deposition, giving rise to poorly controlled film roughness.

Due to overlap of mica and calcite XRD peaks, XRD patterns were measured for films on Au-coated substrates. In most cases, the deposited $CaCO_3$ phase was calcite. Crystallinity and orientation, and most likely morphology, of calcite films varied with deposition temperature **(Figure 3A)**. At 250 °C, XRD revealed two distinct grain orientations with (006) or (104) calcite planes parallel to the substrate. At 300 °C, most of the deposited films were (104)-oriented, with some samples having additionally (006)-oriented grains. At 350 °C, (104) orientation was prevailing. Additional, low-intensity peaks were measured at 2θ of 20.9° and 42.7° for a few samples, which could be most likely be attributed to (00l) reflections of vaterite **(Table S4; Figure S10)**. It is possible that a small amount of amorphous $CaCO_3$ was present in the crystalline films, the quantity of which was likely to decrease with the deposition temperature, as suggested by Nilsen, et al. [44]. Only the films with distinct calcite XRD diffraction peaks were used in the SFA experiments, however the peaks intensity could be affected by presence of µm-sized aggregates. Thickness, thickness gradients, detailed deposition parameters and XRD patterns of all films are provided in SI (**Tables S2, S3, S4; Figure S10**).

As the substrate can influence orientation, crystallinity [44], and $CaCO_3$ phase, it was possible that mica-deposited films were not composed of calcite. Raman spectroscopy of mica-deposited films revealed a single band centered at 1088 or 1089 cm^{-1} (grown at 250 and 300 °C, respectively; **Figure 3B**). This shift

corresponds to the symmetric stretching vibration mode of carbonate groups v1 $(CO_3)^{2-}$, and could be attributed to calcite or, less likely, aragonite [54-58]. Nevertheless, the rhombohedral morphology observed with SEM **(Figure 2A)** was typical for calcite and presence of aragonite was unlikely. No vaterite (with a split v1 band at 1090 and 1075 cm^{-1} [59]) nor amorphous $CaCO_3$, (with a broad v1 band at ~1077–1082 cm^{-1} [60]) were evidenced. The latter, however, could be related to insufficient thickness of calcite films (200 nm).

Topography of Au- and mica-deposited calcite films was measured with AFM (see **Tables S9, S10**). Rms roughness varied within 2 orders of magnitude, and increased with the increasing scan size (*ss*) because of presence of larger polycrystalline asperities (<1 µm; **Figure 4)**. Mica-deposited films exhibited smaller rms values (0.9 nm (*ss* = 0.2 µm) ≤ rms ≤ 109 nm (*ss* = 40 µm)) than films on the initially rougher Au-coated substrates (3 nm (*ss* = 0.1 µm) ≤ rms ≤ 202 nm (*ss* = 5 µm)). On average, films grown at 250 and 350 °C were smoother (max rms = 8.0 nm, *ss* = 10 µm; rms = 17 nm, *ss* = 20 µm, respectively) than the ones at 300 °C (max rms = 202 nm, *ss* = 5 µm). However, we prepared most of the films at 300 °C and we measured small rms values for this temperature as well. Distribution of surface asperities was not homogenous. Average radius of the highest asperities was ~0.5 µm for the roughest surfaces, and ~10 nm for the smoothest surfaces (rms <3 nm). Rms of the films after SFA experiments (**Figure 4**) in $CaCO_3$-solutions did not show a large variation with the scan size as the films before the SFA, and they were in the higher range of all the measured values. Due to high heterogeneity of the films we did not have any precise information of the roughness of contacts established for the SFA measurements, as it was not feasible to locate these contacts on the sample after the SFA, and as their roughness was evolving in contact with water.

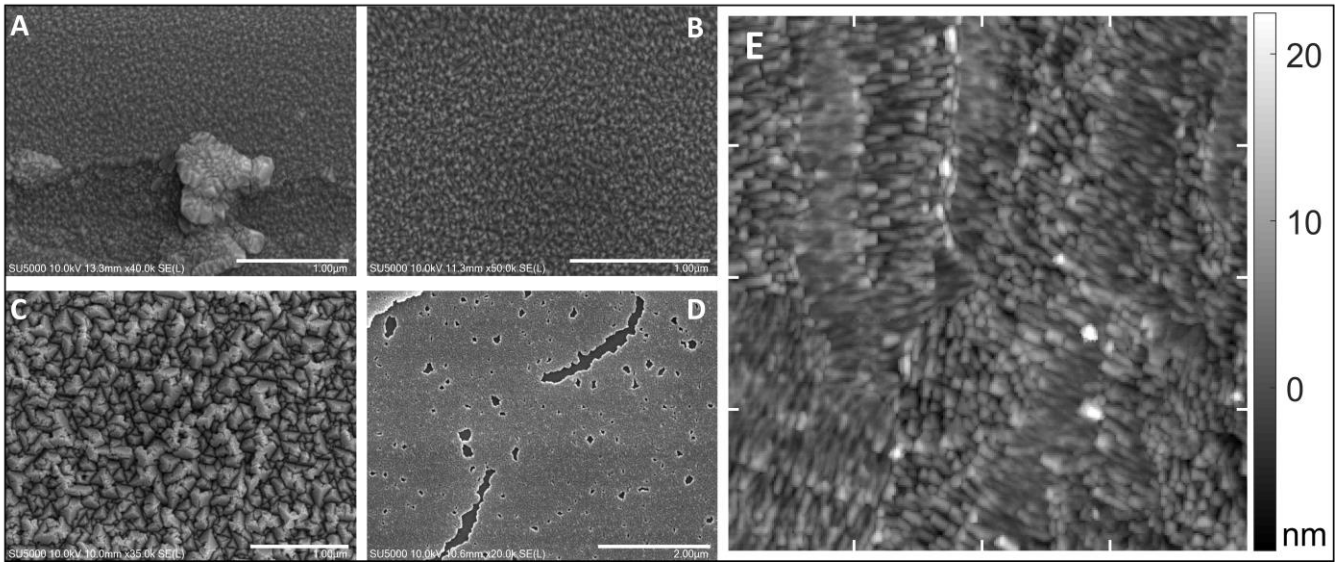

Figure 2. *SEM SE images of the initial (A, B) and final (C, D) topography and AFM height measurement (E) of polycrystalline calcite films deposited on mica (A, B, C, D) and gold (E) substrates: A. 1 µm size asperities, present on some of the surfaces, were polycrystalline (ALD10, 300 °C); B. average size of crystals was smaller than 50 nm (ALD10, 300 °C); C. region with roughened crystals after the SFA experiment (CM350A; ALD13); D. region with dissolved areas after the SFA experiment (CC350A; ALD13). E. AFM of the 200 nm-thick film deposited at 250 °C (scan size 4x4 µm, ticks every 1 µm, rms = 3.9 nm, ALD1). The scale bar is 1 µm (A, B, C) or 2 µm (D).*

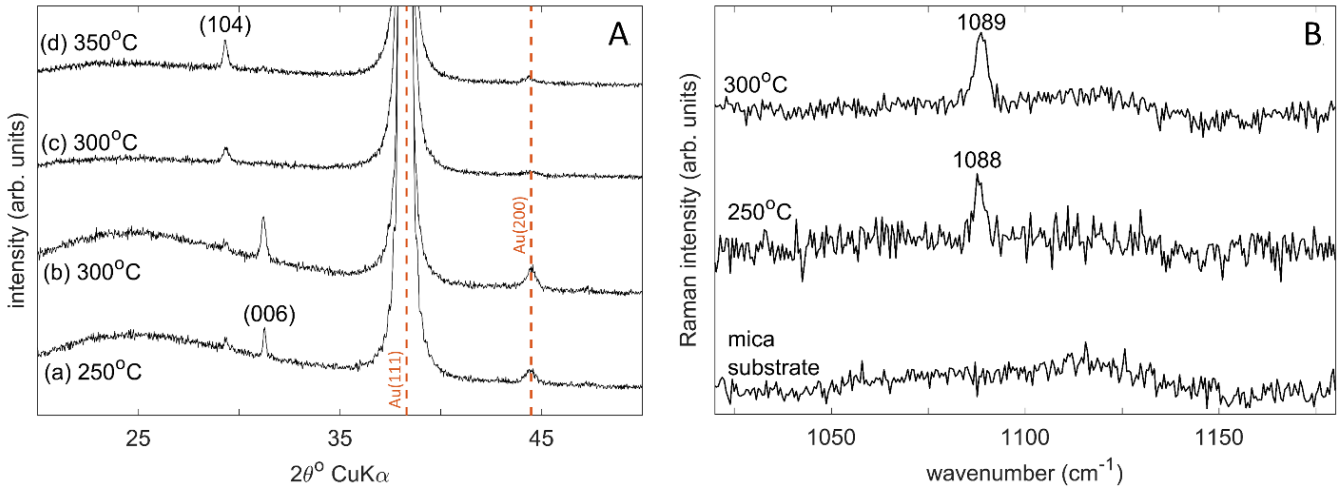

Figure 3. *A. XRD of the chosen calcite films deposited at 250, 300, and 350 °C on Au-substrate: samples a. ALD1 (200 nm), b. ALD2 (200 nm), c. ALD10 (100 nm) and d. ALD13(100 nm). B. Raman spectra of a bare mica substrate and calcite films deposited on mica at 250 and 300 °C (samples ALD1 and ALD2, respectively).*

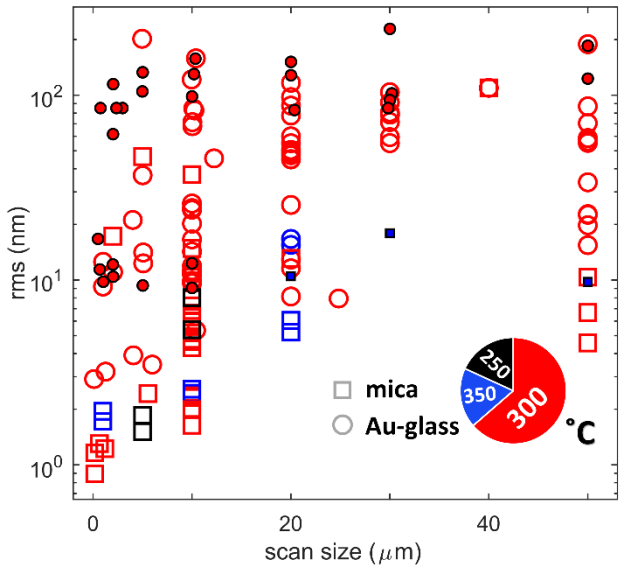

Figure 4. *AFM-measured roughness of calcite films as a function of scan size. Blue, red and black colors correspond to calcite film deposition temperature. Empty symbols represent measurements in air after film deposition (max. 2 weeks). Filled symbols represent measurements for calcite surfaces used in the SFA experiments in $CaCO_3$-saturated solutions. □ – films on mica substrates; or ○ – on Au-coated glass substrates.*

Equilibration of calcite films with solution

We followed initial equilibration of calcite films with $CaCO_3$-saturated solutions both in the AFM **(Figure S23)** and in the SFA (**Figure S17;** solution parameters in **Table S8**). AFM measurements with single, unconfined calcite surfaces did not indicate any significant recrystallization or formation of larger crystals for any of the samples within 1 h. Roughness of the films increased slightly with time (the highest increase in rms was 24 nm; ALD2, 300 °C). The initial and final sample topographies are shown in **Figure S23**.

In the SFA, the equilibration process was followed for two surfaces kept in contact under constant, moderate applied load (<850 mN/m, corresponding to ~5.5 MPa for two smooth surfaces with a contact area radius of 100 μm). We observed that films grown at 250 °C underwent significant recrystallization, whereas the depositions at 300 and 350 °C yielded much more stable films **(Figure S17)**. The much more pronounced reactivity of the 250 °C calcite films was manifested by their rapid dissolution both in air (in the surface adsorbed water film; ~0.2 nm/s) and in the solution (~0.8 nm/s). Dissolution of the 250 °C films continued until much larger (>5 μm) calcite crystals, with dominant {104} faces, rapidly formed everywhere on the sample (after 2 to 40 min since solution injection in different experiments), and replaced the polycrystalline films **(Figures S15, S17D)**.

We expect initial dissolution of all ALD calcite substrates upon first contact with the $CaCO_3$-presaturated solutions since: (1) the solutions were equilibrated with calcite under low CO_2 partial pressures and after filtering, they were slightly undersaturated **(Table S8)**; (2) synthetic calcite crystals in ALD have higher solubility than bulk calcite due to their small initial sizes (>50 nm) and high roughness as follows from Kelvin equation [61], and possibly unstable morphology as they were grown from vapor phase. The latter is related to the observed major recrystallization of 250°C films, driven by the surface free energy minimization (Ostwald ripening [62]): nm-sized crystals were likely bounded by less stable, high-energy {108} planes, as suggested by prior studies[44], and as supported by our XRD results that indicated a different orientation of calcite crystals in these films **(Figure 3)**. Thus, these films dissolved much faster

than the 300 °C and 350 °C films (with crystals most likely bounded by low-energy {104} planes, as suggested by SEM, XRD and previous studies [44]). High reactivity of the 250 °C films could be additionally affected by minor amounts of amorphous $CaCO_3$ and traces of unreacted ALD precursor [44].

Owing to limited diffusion out of the gap between surfaces in a confined SFA geometry and a high flux of ions (10^5 mol·m^{-2}·s^{-1}) leaving the dissolving samples, a supersaturated boundary layer could develop near the 250°C films much faster than for 300 and 350 °C films. Following the calculations in Renard, et al. [63], we estimated that equilibrium thickness of such boundary layer could be tens of µm and could develop within seconds **(SI, S8)**. Since the initial separation between surfaces was much smaller in the SFA, supersaturation threshold in the gaps could be quickly reached for the dissolving 250 °C films, which led to rapid growth of more stable >5 µm crystals on the surface. As the concurrent AFM analysis of a single 250 °C calcite surface showed no growth of the bigger ~5 µm-sized crystals in the solution, we suggest that the confined SFA geometry primarily contributed to this process due to the limited diffusion out of the gap in the normal direction. Since other effects such as applied pressure may influence the recrystallization of calcite films in the SFA, the detailed analysis of these processes is beyond the scope of this paper.

As a consequence, the following SFA force measurements were performed with calcite samples with two distinct topographies: 1) discrete, >5 µm-sized, overgrown calcite crystals bounded by distinct {104} planes (250 °C films); 2) continuous calcite films composed of nm-sized crystals with inhomogeneous distribution of surface asperities and various amounts of larger polycrystalline asperities as in **Figure 2A** (300 and 350 °C films). Thus, >5 µm-sized crystals with relatively flat and smooth faces could yield much higher actual contact areas in force experiments, unlike the nm-sized surface asperities in more stable films, which could only form discrete contacts within the nominal contact area.

Reactivity of Calcite Films During SFA Force Measurements in $CaCO_3$-saturated solutions

Reactivity and thickness of calcite films was followed throughout the SFA force measurements (~25 h): initially, when $CaCO_3$-saturated solution was injected into the SFA while the surfaces were kept in contact under a constant load (I), during the force measurements (FR– loading-unloading cycle), and while keeping the surfaces in contact overnight (T; ~10 h) under a constant applied load (detailed parameters in **Tables S7, S8**). We followed changes in a hardwall position (HP – a smallest separation between the surfaces at a given maximum load) with time in two configurations: in an asymmetric system, with one atomically smooth mica surface against a rough calcite layer (CM; **Figure 5**), and in a symmetric system, using two rough calcite surfaces (CC; **Figure 6**). The changes in HP were used to estimate changes in calcite thickness with time, and high initial HPs were due to large asperities on surfaces **(SI, S1.3)**.

Within first 0.5 h, when surfaces were kept in contact (I), dissolution in CC occurred to a much bigger extent than in CM, even if accounted for two calcite layers in CC **(Figures 6D, E; S18, S19).** We do not quantify these dissolution rates precisely due to variations in: initial temperatures (22 – 26 °C); changes in temperature (0.02 – 0.3 °C); initial pH of solutions (8.5 – 9.9); initial saturation index of solutions with respect to calcite (-1.0 – 0.1); applied loads (18 – 746 mN/m); contact areas (<<0.03 mm^2); and resulting pressures (>>0.01 MPa; minimum pressure estimated for smooth surfaces in a contact of 100 µm radius under 18 mN/m applied load). Despite these variations, we observed a major difference in HP shifts between CC and CM **(Figures S18, S19)**. The HP in CC always decreased within the first 0.5 h (2 – 488 nm/h in 11 experiments). In CM, decrease in HP was evidenced in 2 experiments (3 - 25 nm/h) and an increase in HP for 4 of them (1 – 858 nm/h). The highest increase in CM corresponded to the most reactive DS films **(Figure 5A).** Calcite dissolution was generally faster for thicker initial gaps between surfaces (apart from surfaces with very large asperities in contact regions; **Figure S18),** and slower for smoother contacts (**Figure S19**; contact roughness λ estimated from FRs as in **Figure 7**).

Within 25h, we observed distinct behavior of the discontinuous substrates (DS) with >5 µm-crystals and the continuous nanocrystalline films (CS). After the rapid recrystallization, DS showed progressive growth of µm-sized crystals **(Figure 5A)**. CS generally dissolved or grew only slightly but the calcite coverage remained continuous (partial pitting could be sometimes observed on sample edges; **Figure 2D)**. For CS, major shifts in HP occurred during FRs, when the surfaces were constantly brought in and out of contact, with less changes during *T*. HP shift depended also on surface configuration: in CC, the surfaces generally dissolved throughout the experiments, but for some experiments could grow after a few hours **(Figure 6E, G)**; in CM, surfaces dissolved to a much smaller extent, and could sometimes grow initially **(Figure 5A, C, E),** and grow markedly in later stages **(Figure 5B, E).**

Additionally, both in CC and CM, major recrystallization events were sometimes observed after several hours, when two surfaces were kept constantly in contact (during *T*). In such events, crystals growing in or near the contact region were found to push the opposing surface away, despite applied loads <200 mN/m (**Figures 5B, E; 6E, G**). Such extensive recrystallization took place only for the least rough contacts, where real contact areas were the largest, and the surfaces could be approached very close to each other (121 nm > initial HPs > -7 nm). These events were not correlated with temperature increase, and therefore were not caused by decreasing calcite solubility. As the used solutions were slightly undersaturated with respect to calcite **(Table S8)**, any significant growth of calcite layers was not expected. Because all the major recrystallization events were preceded by a small decrease in calcite thickness (HP shifts between -8 and -47 nm), we suggest that the subsequent rapid roughening of calcite was triggered by increasing supersaturation in contact regions, due to prolonged calcite dissolution and limited diffusion from the contact regions to the bulk. In CM, where adhesive forces between surfaces were measured, recrystallization of smoother contacts **(Figure 5A, B, D, E)** could lead to significant roughening, decrease in contact areas and resulting absence of adhesion **(Figure 5E).** In such cases, two surfaces separated by growing crystals showed a small jump-out, followed by the surfaces drifting out of

contact **(Figure 5E).** Less frequently, rougher mica-calcite contacts evolved into smoother, adhesive contacts by ripening growth of some asperities and a resulting increase in the real contact area **(Figure 5D).** The morphology of a calcite film that underwent a significant recrystallization is shown in **Figure 2C**, indicating an area with coarser and more irregular crystals. Such coarsening was evidenced only in some regions of the samples and it was not possible to distinguish where the SFA contact regions were. In the following we discuss how contact topography, pressure distribution across contacts, and presence of mica in asymmetric systems might have affected calcite reactivity in the SFA.

Effect of Contact Topography and Applied Load

Apart from initial crystal morphology (as discussed in the previous section), topography of contacts had a major influence on calcite dissolution, growth and recrystallization during SFA experiments. This is supported by two major observations: (1) calcite dissolved more slowly for smoother contacts and for thinner gaps between two surfaces **(Figures S18, S19)**; (2) major recrystallization events were observed only for the smoothest contacts **(Figures 5B, E; 6E, G)**. Since all the surfaces were prone to initial dissolution upon equilibration with solutions, the observed correlations were most likely related to degree of confinement that affected mass transport along the contact. Diffusion from the gap (where concentrations of ions was momentary higher due to high flux of dissolving species) to the bulk was not only affected by the limited transport in the normal direction, but also by the roughness of contacts. Models of a gap distribution in contacts between a randomly rough surface against a smooth, elastic surface predict the existence of contact and non-contact patches that display different fluid percolation properties [64]. Thus, we may expect saturation gradients in the voids between contacting asperities. As we followed changes in calcite thickness only in a small region of nominal contact area in the SFA, dissolution or growth in our system was only an average result of volume change of all the small crystals within this contact. Since we could not precisely quantify the roughness in SFA contact regions (the used calcite films were heterogenous and their rms roughness could vary over almost two orders of magnitude for AFM

scan size 50x50 μm^2; **Figure 4**), we do not undertake to estimate real contact areas in our system. However, we expect that voids areas in contact regions were generally larger for two rough surfaces in CC than in CM with one smooth surface and that they were proportional to initial gap thickness (surfaces were heterogenous, and contacting them in a commensurate manner, so that asperities could interlock each other, was unlikely). Saturation with respect to calcite should be thus achieved faster for smaller volumes of these voids in CM, which is in line with our observations **(Figures S18, S19)**.

Dissolution of rough calcite surfaces in contact was very likely affected by the applied pressure. Pressure may (1) enhance dissolution due to pressure solution, and (2) cause plastic deformation of calcite crystals. Pressure enhances the solubility of the stressed solid, driven by an increase in chemical potential relative to a stress-free surface [65]. Due to roughness, the stress distribution in our system was inhomogeneous [66]. If we assume that real contact areas in CC were generally smaller than in CM, the stress transmitted at these discrete contacts in CC would be much higher [67] than in CM under the same load. We would therefore expect larger volume changes due to pressure solution in the CC system. Although this is what we observed **(Figures S18, S19)**, it was not possible to quantify the dissolution due to applied stress. Because of the surface roughness, we did not observe any correlation between applied load and dissolution rate.

With the used range of loads (>850 mN/m), the pressure at the highest asperities most probably exceeded 1 GPa (at which plastic deformation of single calcite crystals has been observed [68]). Any possible plastic deformation of calcite surfaces would be expected to take place when the surfaces were first pushed into contact [25]. The decrease in thickness progressing with time, observed also during unloading **(Figures 10, S20),** cannot be thus explained by plastic yielding. However, it was highly likely that plastic deformation of the highest asperities took place on the initial loading, leading to an irreversible deformation and flattening of these asperities.

Effect of Dissimilar Surfaces

Much less pronounced calcite dissolution in CM **(Figure S18)** could have been additionally affected by the proximity of mica surfaces. The mica basal surface is negatively charged (σ = ~-0.3 C/m^2) and the near-surface distribution of counterions, such as Ca^{2+}, can be many times higher than in the bulk. Higher valency ions preferentially adsorb on the surfaces [25], and their exchange with other species from the bulk is very slow [69-70]. The initially dissolving calcite could be a source of Ca^{2+}, which upon binding to mica might have contributed to the supersaturated conditions in the gap. Å-size $CaCO_3$ crystals have been reported to grow between mica surfaces separated by <1 nm, even in undersaturated bulk conditions, and calcite has been observed to grow between mica layers in nature [70]. This suggests that mica can promote the growth of calcite, in contrast to silica enhancing the dissolution of halite [71] or mica enhancing the dissolution of quartz [72]. Dissolution in the latter system has lately been attributed to electrochemical corrosion interactions in the electrical double layers of these dissimilar surfaces [73-74]. In our experiments, there was a difference in surface potentials (ψ_0) of mica (~-70 mV; **S5, Figure S13**) and calcite (~-20 mV, [24, 75]) in $CaCO_3$-saturated solutions. If the recrystallization of calcite in the proximity of mica could be triggered by an overlap of the electric double layers of these two minerals [73], it would rather be expected that the dissolution of calcite (higher ψ_0) was enhanced by mica (lower ψ_0). In such case Ca^{2+} transfer would take place from calcite to mica, and perhaps induce calcite precipitation on mica. This possibility could not be ruled out in FECO (not possible to distinguish on which surface the process took place), nor with SEM after the SFA experiment (crystals could be too small). However, we observed a strong attractive interaction in CM (also for growing calcite surfaces), which was never present in CC [23]. This indicates that calcite did not nucleate on mica, at least not in the contact region, as this would have led to an absence of attraction. If mica does enhance the dissolution of calcite, then the observed growth had to be caused by the resulting supersaturation conditions in the gap between the surfaces. The growth of the calcite

layer was rather limited (several nm/h), and we suggest that the observed growth was a result of dissolution/precipitation in the gap [76].

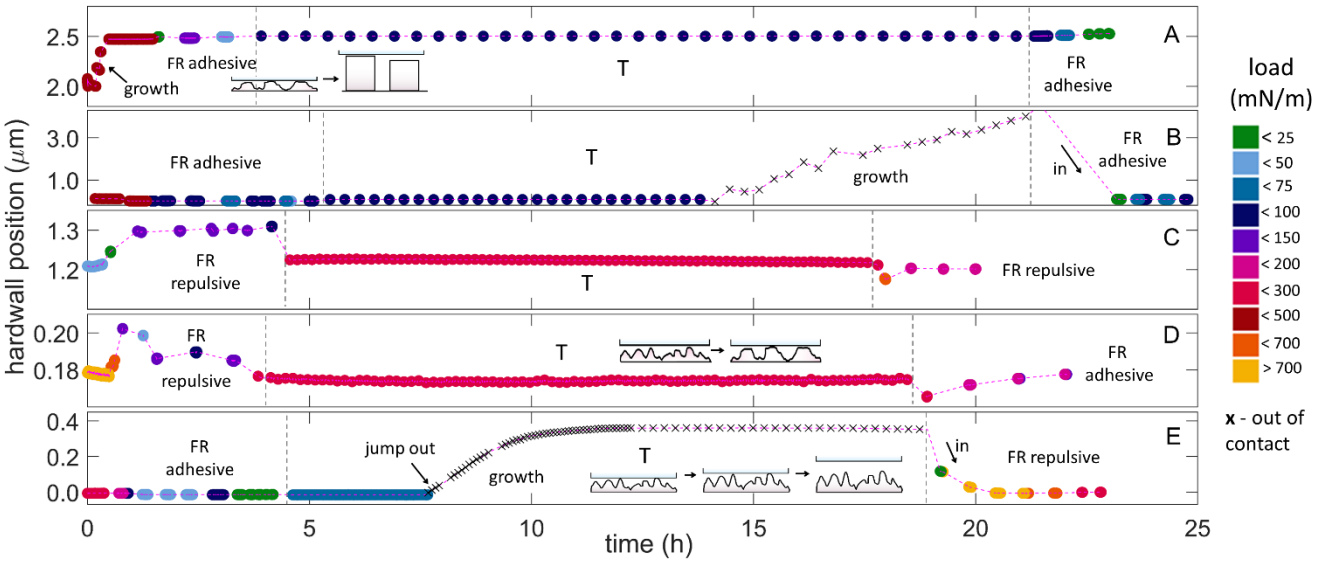

Figure 5. *Evolution of hardwall position (HP) with time in SFA experiments between mica and calcite surfaces (CM) in $CaCO_3$-saturated solution. Major recrystallization events were indicated, where x refers to surfaces separating from contact due to calcite growth. FR – HP measured during loading-unloading cycles with an indication of adhesive or repulsive interaction between the surfaces; T – HP measured while keeping surfaces in contact under constant load. The used calcite surfaces were deposited at different temperatures: A. 250 °C (CM250A; ALD1), B. 300 °C (CM300A; ALD2), C. 300 °C (CM300B; ALD6), D. 300 °C (CM300C; ALD6), and E. 350 °C (CM350A; ALD13). Note large differences in y axes scales.*

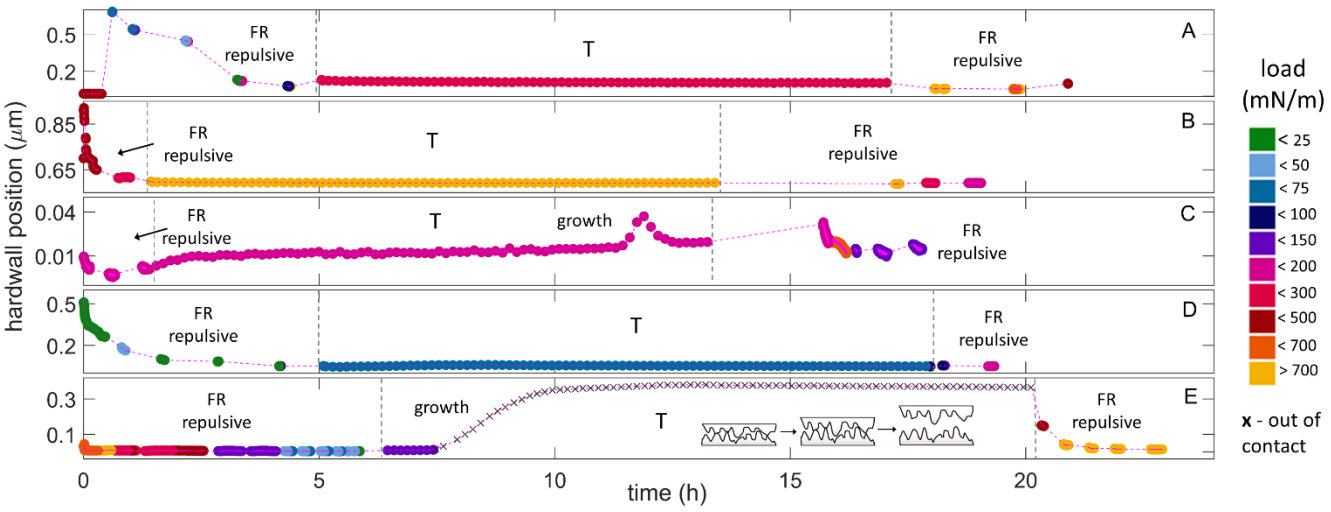

Figure 6. *Evolution of hardwall position (HP) with time in SFA experiments between two calcite surfaces (CC) in $CaCO_3$-saturated solution. FR – HP measured during loading-unloading cycles; T – HP measured while keeping surfaces in contact under constant load. The used calcite surfaces were deposited at: A. 300 °C (CC300B; ALD4), B. 300 °C (CC300C; ALD5), C. 300 °C (CC300A; ALD6), D. 300 °C (CC300D; ALD10), and E. 350 °C (CC350A; ALD11).*

Force Measurements Between Calcite and Mica Surfaces

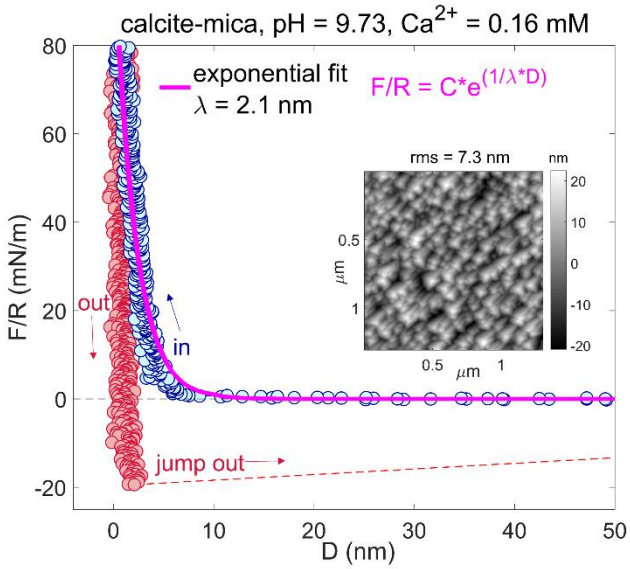

Figure 7. *Representative data from SFA measurement of forces (normalized by contact radius, F/R) between calcite and mica surfaces as a function of separation (D), showing an adhesive interaction in a $CaCO_3$-saturated solution. D values were shifted so that HP = 0 nm at the maximum applied load. Pink line shows an exponential fit to the FR on approach, F/R = C·exp(1/λ·D), used to estimate a roughness magnitude, where λ is an exponential decay length, proportional to average local roughness in contact region. Inset shows an AFM height map of the calcite film before the experiment (CM300A, ALD2, rms = 7.3 nm).*

Forces in asymmetric CM setups were measured in $CaCO_3$-saturated solutions **(Table S8)**. Both adhesive and repulsive forces were observed in CM, depending on the calcite surface topography. Adhesive forces could be measured whenever a sufficiently large contact area was established between the surfaces, which usually corresponded to the least rough calcite surfaces. Additionally, adhesive forces were observed both with DS (>5 μm crystals) and CS calcite substrates. A representative adhesive FR in CM is shown in **Figure 7:** forces on approach were in most cases purely repulsive, with no resolved jumps-in, followed by relatively large adhesive jumps-out on separation. The magnitude of pull-off forces varied between consecutive FRs in each experiment, suggesting an evolution of contact topographies with time.

Adhesion was present both when the calcite layer was growing (CM250A, CM300C) and dissolving (CM300A, CM350A).

Adhesive Interactions in CM

We measured strong pull-off forces in CM. From comparing the theoretical VdW interaction in CC, in CM and between two mica (MM) surfaces, VdW attraction should be slightly higher in CC and almost the same in CM and MM (Hamaker constants of 1.44, 1.35 and $1.34 \cdot 10^{-20}$ J, respectively [77]; see **SI, S6**). We measured weaker pull-off forces in CM than in MM **(Figure S14)** in $CaCO_3$-saturated solutions, which is most likely due to calcite roughness and much smaller contact areas in CM. The average pull-off force in MM was 85 mN/m (varied between 61 and 11 mN/m in 6 experiments; data not shown), whereas in CM it ranged from 0.1 to 26 mN/m, depending on the roughness. The strongest adhesive force in CM was thus only ~3 times smaller than in MM. Since we assume that even for the smoothest calcite surfaces the real contact area was only a very small fraction of a nominal area in the SFA, we would expect the adhesive force and adhesion energy to be even weaker in CM, if the attraction was only related to VdW interaction. Therefore, it is likely that other non-DLVO attractive effects were also present. According to zeta potential measurements [24], at high ion concentrations (that could be present due to dissolution of calcite and a higher concentration in the gap between the surfaces) the calcite surface can become positively charged, while the mica surface is still negatively charged, leading to a longer-ranged electrostatic attraction of the double layers. Additional electrostatic effects, such as ion correlation forces, could also enhance the adhesion in CM. These interactions are particularly strong in presence of higher valency cations (e.g. Ca^{2+}) even in dilute solutions, and are possibly responsible for limited swelling of Ca^{2+}-clays [25, 78-80]. The magnitude of electrostatic effects was likely affected by roughness as the distance between surfaces and distribution of ions was disrupted due to variation of surface heights in contacts.

Effect of Reactivity and Applied Load on Pull-off Forces

We investigated how the measured pull-off forces corresponded to the changing topography of calcite within 2 days **(Figures 8, 9)**. Since both the magnitude and onset of attractive and repulsive forces

will depend on surface roughness [32, 43, 81-83], we used an exponential decay length λ of the approach part of the repulsive FRs to semi-quantify the changes in surface roughness, according to $F/R = C \cdot \exp(1/\lambda \cdot D)$ **(Figure 7)**. We assume that in our system, the major contribution to the measured repulsive forces is the energy needed to compress multiple surface asperities elastically, which can be represented with a Hertzian-type deformation [25, 34]. As such, λ should be proportional to the average local roughness of the contact areas (involving only the asperities 'felt' by the approaching surface upon loading), but not to the overall rms roughness of the samples [84]. Even though the measured FRs did not always show a purely exponential behavior on approach (which is typical for rough surfaces with a random, Gaussian-like distribution of heights [34, 81]), λ was still a satisfactory parameter to account for the magnitude of changes. We expect EDL forces in our system to have a minor contribution to the measured repulsion (theoretical EDL forces for smooth CM surfaces in a $CaCO_3$-saturated solution are long-ranged, with the onset at >70 nm, and of very low magnitude; EDL_{max} <6 mN/m; see Eq. S4; onset refers to distance at which the magnitude of force is significant). The repulsion could be affected by the hydration force, as discussed later.

In general, adhesive forces in CM were detected for FRs with the decay lengths λ on approach <8.5 nm **(Figures 8A, 13)**. The pull-off forces increased with decreasing λ, and thus with smaller roughness of calcite in contact regions. This dependence was not apparent for CM250A; however, the topography of these recrystallized samples differed a lot (>5 µm-sized crystals; **Figure S15**) in comparison with continuous films. Thus, the resulting real contact areas for CM250A could be much bigger, and the measured pull-off forces were more dependent on the applied load (much weaker adhesive forces in runs 2, 4, 5 clearly corresponded to applied load values <50 mN/m; **Figure 8B**). There was no correlation between the maximum applied load and the magnitude of pull-off forces for the other experiments (CM300A, CM300C, CM350A). There was also no link between the maximum applied load and roughness (λ) change **(Figure 9A).**

Pull-off forces varied with experimental time **(Figure 8A),** and became stronger in consecutive FRs for all experiments, both for dissolving (CM300A, CM350A; **Figures 5B, E**) and progressively growing calcite (CM300C and CM250A; **Figures 5D, A**)**.** This suggests that the adhesive forces were affected by changes in contact topographies, which could become less rough with time. Consequently, the contact areas and the pull-off forces increased. Evolution of contact roughness (λ) with time is shown in **Figure 9B**. In all cases, we observed an initial decrease of λ within the first 5 h. We did not have information about the roughness evolution while the surfaces were kept in contact overnight (5–20 h), but the first measured λ on day 2 increased relative to the last experimental point on day 1 in most experiments (apart from CM250A and CM300C). λ gradually decreased again once the FRs were restarted the following day (20–25 h, except for CM250A and CM300A). At times when λ was progressively getting smaller in consecutive FRs, we mostly observed a corresponding gradual decrease in HP (CM350A, CM300B, CM300A, CM300E) or less frequently an increase in HP (CM250A, CM300C; **Figure 9C**). The magnitude of these HP shifts rarely exceeded 100 nm and they were related to average behavior of many asperities within the nominal contact regions. This shows that during FRs, the contact topographies could become smoother both in case of dissolution and growth of calcite layer, and suggests that not directly the surface reactivity, but the repeated loading of the surfaces could significantly contribute to gradual decrease in roughness at the contacts. This is further supported by the fact that during periods when the surfaces were constantly kept in contact overnight (*T*) and no loading-unloading cycles were performed, the roughness increased in most experiments.

We thus suggest that the increase in pull-off forces and decrease in roughness during FR was related to pressure deformation of calcite asperities, and not directly to calcite dissolution or growth due to changes in chemical equilibrium in the gap between surfaces. The applied load could affect the pull-off forces in two ways: (1) increase the real area of contact reversibly by elastic deformation; (2) influence the real area of contact irreversibly by pressure solution and plastic deformation.

Firstly, for multi-asperity rough elastic surfaces, higher applied loads yield proportionally larger real contact areas [85-87], likely to result in higher adhesion energies and thus higher pull-off forces. Pull-off force is also affected by roughness in another way: elastic energy on compressing the asperities is released during the unloading and may be large enough to overcome the adhesive bonds [83], sometimes counteracting the expected increase of the adhesion force due to a higher real contact area [84]. Reversible elastic deformation of asperities cannot however explain the progressive increase in adhesion forces with time.

Secondly, the applied load could induce irreversible changes in the contact topographies. Pressure solution favors dissolution of the highest, most stressed asperities in contact over the stress-free non-contact regions, because of the differences in their chemical potential. Similarly, the highest asperities could be plastically deformed on repeated loading. We could not distinguish between these two pressure-driven mechanisms unambiguously. However, using the plasticity index (PI) parameter [82, 88], it is possible to estimate if an elastic or a plastic mode of deformation of the rough surfaces is dominant. PI is based on hardness, elasticity and roughness parameters for a given surface, and is calculated as: $PI = \frac{E_r}{H}\sqrt{\frac{\sigma_h}{r_h}}$, where E_r is the reduced Young's modulus (see Eq. S6), H is hardness, $\sigma_h$is standard deviation of surface heights as measured with the AFM, and r_h is an average asperity tip radius as estimated from the AFM topography scans. PI was calculated for the calcite films using *H* = 1.49 GPa [89], and Young's modulus of 72.35 GPa. For one of the smoothest calcite surfaces (ALD13; σ_h = 4.3 nm, r_h= 55 nm, scan size = 10x10 μm^2) we found PI = 7.4, and for one of the roughest surfaces (ALD6, σ_h = 114 nm, r_h= 520 nm, scan size = 10x10 μm^2) PI = 12.5. Such large values of PI >1 suggest that asperities in the calcite films were very likely to undergo plastic deformation, both for very smooth and very rough surfaces.

If we assume that the effect of pressure is to smoothen the surface [65, 90-91], and the effect of chemical dissolution is to roughen the surface [26, 29, 92-95], we expect pressure to influence the topography, as we see decrease of λ with time. Higher pressure concentration at asperities likely enhanced their

preferential dissolution/deformation. Since the calcite films were prone to plastic deformation, we suggest that contact areas increased due to progressive flattening of the highest asperities on repeated loading-unloading cycles. In conclusion, in all cases we saw an increase of the measured pull-off forces with time related to a pressure-driven topography evolution towards higher contact areas, which was interrupted by the periods of time when surfaces were kept in contact for several hours and became rougher.

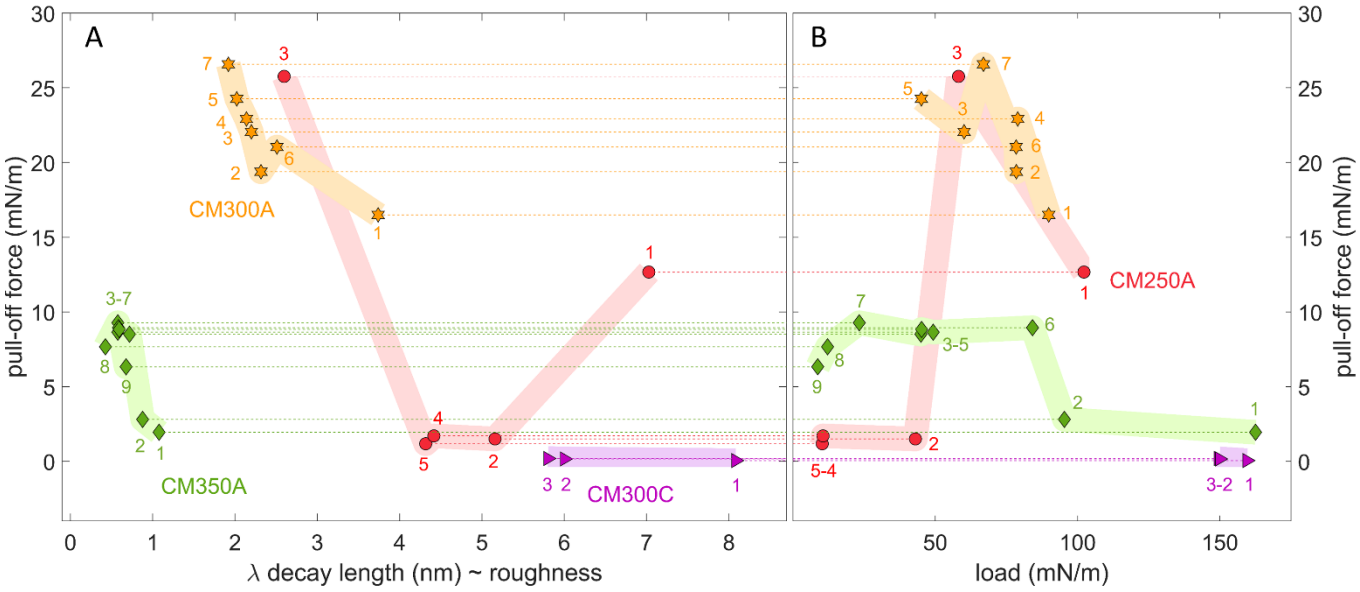

Figure 8. *Pull-off forces (minimum of measured attractive force upon separation) as a function of A. estimated roughness magnitude (λ – exponential decay length), and B. maximum applied load between calcite and mica in $CaCO_3$-saturated solution. The numbers represent the order of FR measurements. Each color corresponds to a different set of calcite-mica surfaces (CM250A – ALD1, 250 °C, runs 1,2 on day 1, runs 3–5 on day 2; CM300A – ALD2, 300 °C runs 1–5 on day 1, runs 6,7 on day 2; CM300C – ALD6, adhesive on day 2, 300 °C, CM350A – ALD13, 350 °C, adhesive on day 1). Horizontal lines connect corresponding experimental points. The pull-off forces (and loads) for CM300C were 1) 0.05 (159.5), 2) 0.16 (149.9), and 3) 0.19 (149.4) mN/m. The absolute magnitudes of forces in different experiments are not comparable due to major differences in contact topographies and areas.*

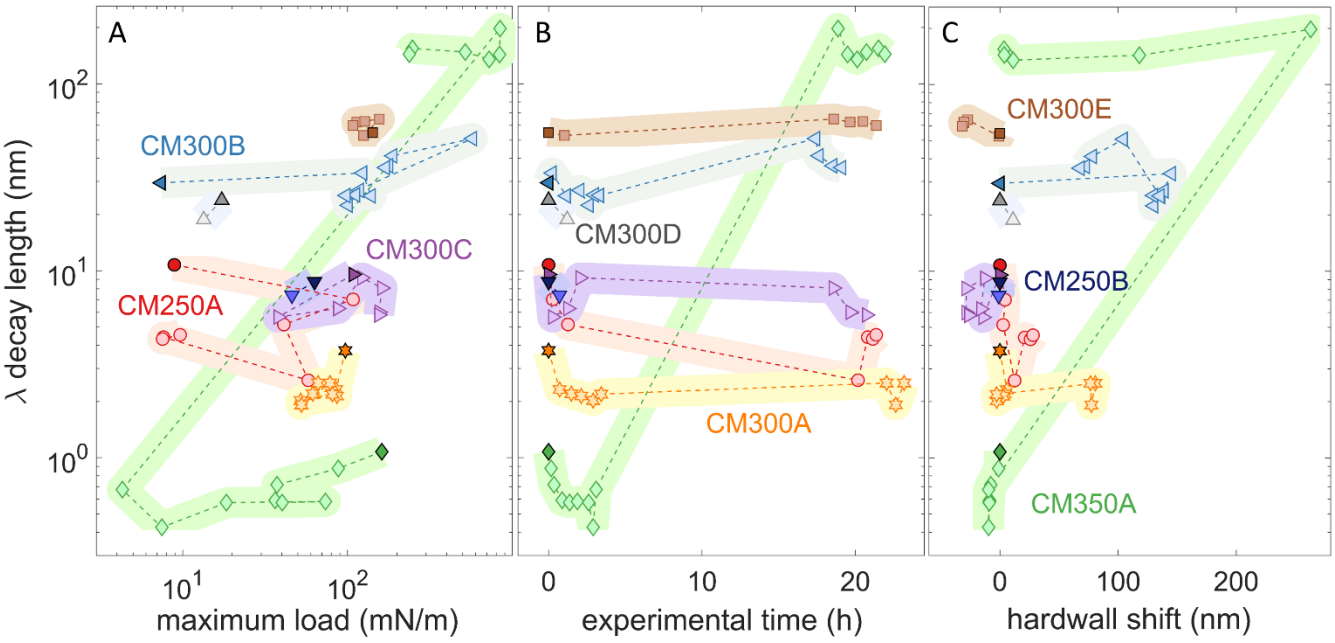

Figure 9. *Exponential decay lengths λ (~ roughness) of the FR curves measured with the SFA on approach between calcite and mica surfaces, as a function of A. maximum applied load, B. experimental time, and C. shift of HP. The shown data includes both repulsive and adhesive FRs. The dashed lines connect the data points in the order of the measurement and the first measured FR curve in each experiment was marked with a darker-colored symbol. The shift in HP position was given with respect to the first experimental point and was measured at the same applied load value for each experiment.*

Force Measurements Between Two Calcite Surfaces in $CaCO_3$-saturated Solutions

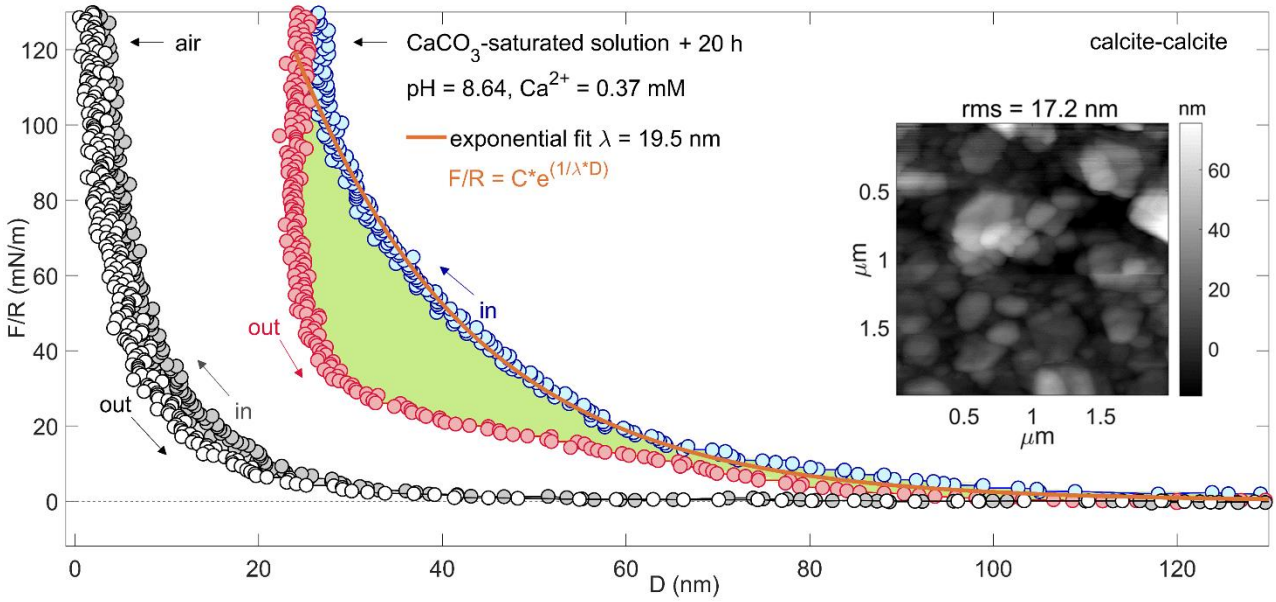

Figure 10. *Representative SFA force-distance curves between two rough calcite surfaces in air and in $CaCO_3$-saturated solution. The D values were shifted so that HP = 0 at the maximum applied load in the FR measured in air with no prior drying with N_2. The shown FR in $CaCO_3$-saturated solution was measured 20 h after the FR in air in the same contact region (within that time FR, T and FR again were performed in solution; see duration of experimental stages in solution in* **Figure 6E***). The green area marks the hysteresis between approach and separation. The inset shows an AFM height map of the calcite film before the experiment (CC300A, ALD6, rms =17.2 nm).*

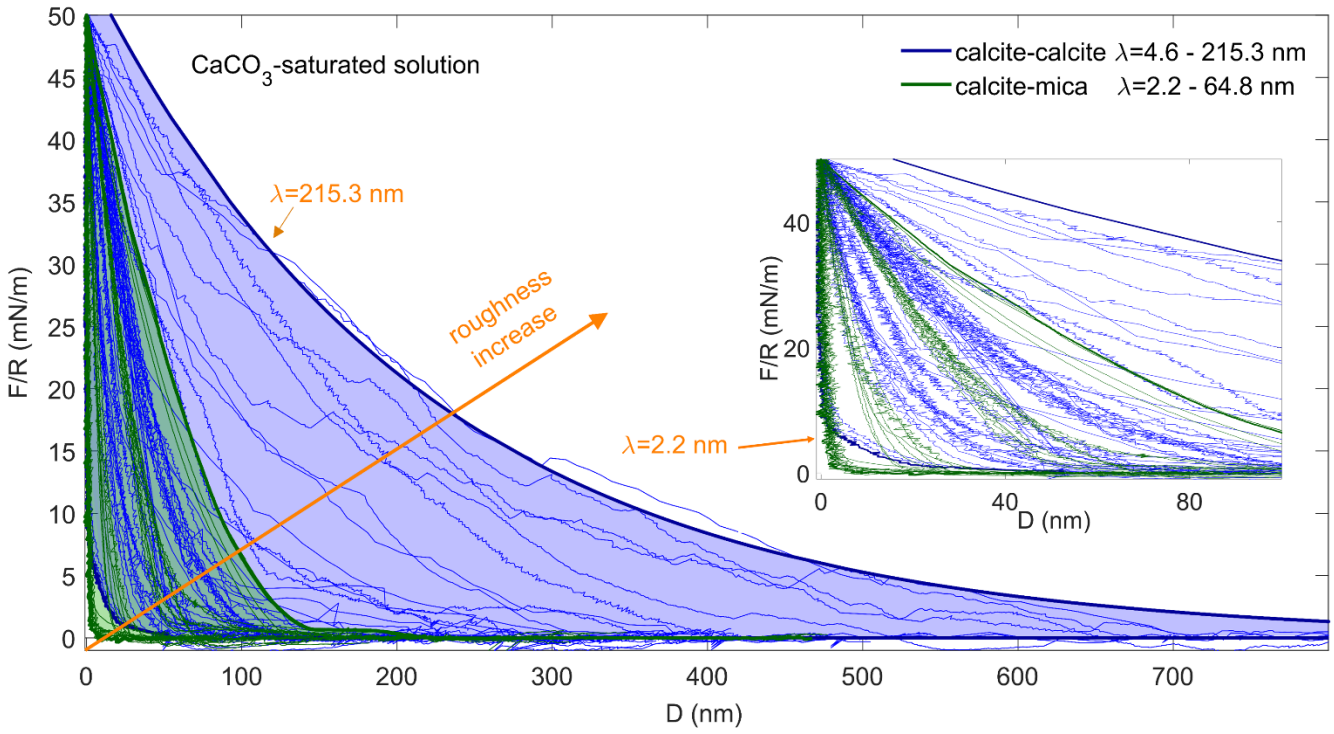

Figure 11. *Repulsive forces as a function of a distance D between two calcite surfaces (11 different sets of surfaces; blue) and between calcite and mica (7 different sets of surfaces; green) in $CaCO_3$-saturated solution. The magnitude and onset of the repulsive forces was strongly influenced by the roughness of calcite films, with exponential decay length λ ranging from 2.2 to 215.3 nm. Only the FRs on approach are shown. The D values were shifted so that D = 0 nm was located at the applied load of ~50 mN/m for all the FRs. The shadings mark approximate ranges of the measured forces. The inset zooms the D region between 0 and 100 nm.*

Forces in CC were measured in $CaCO_3$-saturated solutions **(Table S8)**. We observed only repulsive forces, in solution as well as in air **(Figure 10)**. Whereas the FR in air showed only a small hysteresis between loading and unloading, we observed significant hystereses in the FR measured in solutions. Such hystereses, fully located in the repulsive region of the force, were measured for all experiments in CC (and in CM with no adhesion force). The differences in magnitudes and onsets of the repulsive force and shifts in HP for FRs in air and solution indicated progressive changes in contact topographies of the reactive calcite surfaces. Generally, larger magnitudes and ranges of repulsive force corresponded to higher roughness of contact areas in the SFA **(Figures 11, S21, S22)**. The exponential decay lengths of the FR on approach, used to estimate the local roughness in contacts, varied between 5 and 216 nm for two rough

surfaces in CC, and between 2 and 65 nm for one rough surface in CM. Even though adhesive forces were measured in CM for the surfaces with λ <8.5 nm, we did not measure any adhesion even for the smoothest set of surfaces in CC (λ = 4.6 nm). The rms values of the calcite surfaces measured with the AFM after the SFA experiments ranged from 9 to 228 nm **(Figure 4, Table S10)**, however they did not always correlate well with λ for a given set of surfaces in the SFA, perhaps because it was not feasible to image the same region of the sample. No 'jump-in' discontinuities [24] in the repulsive forces on approach were detected, presumably due to the high roughness of the surfaces, which averages the surface forces, and also due to the low resolution of the FECO in CC **(Figure S3)**.

Repulsion in CC is primarily a mechanical effect, reflecting the energy needed to compress multiple asperities upon loading. After the major recrystallization events, the range and onset of the repulsion increased, mainly because topography of calcite surfaces was altered in a way that more asperities could come into contact. This was related to an overall increase in roughness (higher rms values) but also to the changes in asperity distribution: it was sometimes observed that the least numerous, highest asperities dissolved, and the distribution of surface heights became more symmetrical (see AFM histograms of heights before and after the SFA, **Figure S21**). Repulsive mechanical effects were enhanced when the calcite surfaces were growing, and the resulting force of crystallization[96] counteracted the applied load (e.g runs 12-14 in **Figure S22**). Additionally, there could be some degree of friction between the asperities that mutually aligned in a contact in CC. Dominance of the mechanical effects was previously found to strongly decrease or totally overcome the expected adhesive forces in numerous systems [32-33, 83-84, 97-101].

Repulsion in CC is also most likely influenced by chemical effects, including non-DLVO forces. We evidenced no pronounced EDL repulsion nor VdW attraction. No resolved EDL region (λ_{Debye} ~ 16 nm) was due to roughness, which averaged a distribution of surface species, making the Stern layers more diffuse. No evidence of VdW attraction in FRs might have been additionally related to hydration force apart from

roughness (due to elastic compression and insufficient contact areas). The repulsive forces between two smooth calcite surfaces [23] or between smooth calcite and silica surfaces [24] were only recently measured with AFM and attributed to the hydration effects (which produce repulsive steric forces related to water adsorption on hydrophilic calcite surfaces and to dehydration of counterions populating calcite's Stern layer) [25]. As such, we suggest that hydration could contribute to the repulsion measured in CC, although it was not possible to directly evidence the presence of hydration forces in our experiments. A much lower magnitude of the hydration force is expected for rough surfaces, as only the highest asperities in contact will reach separations small enough to experience this nm-ranged interaction.

Both the hydration force and roughness effects add an exponentially repulsive component to the total force acting between the surfaces, thus it is frequently difficult to distinguish between these two contributions. To account for them in CC, we adapted a model from Parsons, et al. [34] , which incorporates two roughness-related components: 'roughened' DLVO forces and a repulsive contact force due to compression of surface asperities (**SI, S7**). Since apart from DLVO forces, hydration effects likely acted between calcite surfaces in CC, we modified the first model component to include the hydration forces. These forces are reasonably estimated by the following exponential term with small decay lengths (D_H) of a few nm (0.5 – 2 nm), as has been measured for silica and mica [102-104]:

$$\frac{F}{R} = C \cdot \exp(-\frac{D}{D_H}) \qquad \text{(Eq. 1)}$$

where C is an empirical force constant (N/m). The final force fit (Eq. S7) was given as a sum of such 'roughened' DLVO + hydration (Eq. S5) and the repulsive mechanical contact force to due asperity compression (Eq. S6). The roughness and hydration contributions were estimated for a representative experiment in CC **(Figure 12).** We measured long-range repulsion with an onset at ~70 nm from the estimated HP, and the magnitude 100 times higher than the theoretical EDL forces. Assuming rms roughness of both calcite surfaces to be 46 nm (as measured with the AFM but in a different region on a sample), the high-magnitude experimental repulsion could be solely explained by the repulsive contact

force component (Eq. S6, **Figure 12e**). When the hydration repulsion was included (D_H = 0.5 nm, C = 110 mN/m, Eq. 1, **Figure 12f**), the contact force contribution could be accordingly smaller. Because of the uncertainty in rms values at the contact established in the SFA, it was not possible to precisely distinguish between the hydration and the contact force contributions. Most of the repulsive effects in CC could be thus attributed to a mechanical work needed to compress the surface asperities, and this repulsion was likely enhanced by the dehydration of the highest, contacting surface asperities.

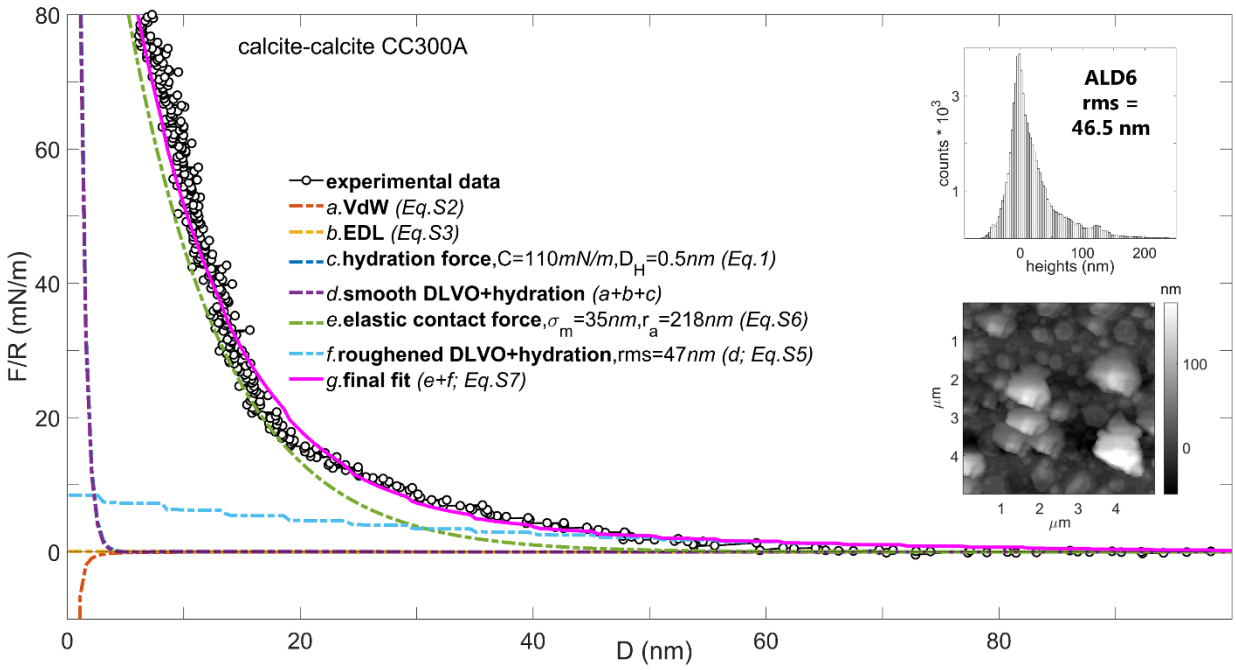

Figure 12. *Modelling of the roughness contribution to the total forces between two calcite surfaces. The final fit (solid line) was a sum of the elastic contact force and the roughened DLVO + hydration forces (Eq. S7; c. and d. contributions are overlapped). Insets show AFM-measured histogram of height and topography of the used calcite film in air (ALD6).*

Loading-Unloading Hystereses

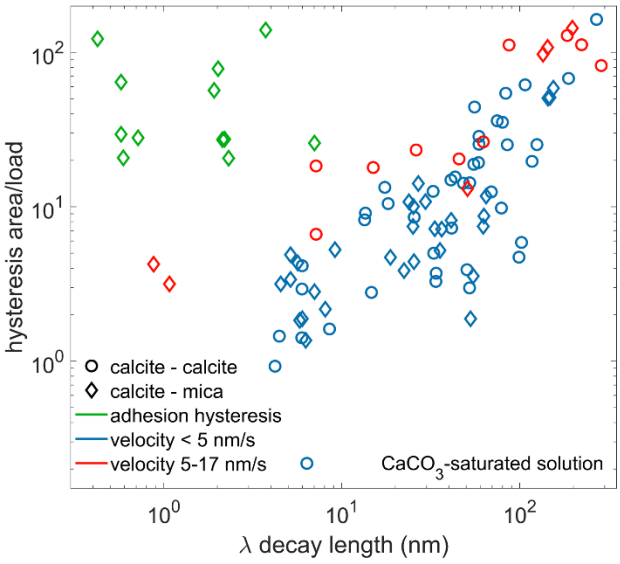

Figure 13. *Area of hysteresis between FRs on approach and on retraction as a function of exponential decay length λ (~ roughness) of the FRs on approach, for calcite-calcite (9 sets) and calcite-mica (7 sets) surfaces. Areas of hystereses were normalized by maximum applied load (mN/m) at which the hystereses were still present and were not corrected for calcite dissolution/growth. Green color corresponds to adhesive FRs between mica and calcite, with areas calculated both in attractive and repulsive regions of FRs. Red and blue colors correspond to repulsive FRs, with hystereses fully located in the repulsive region of the FR curves (as in* **Figure 10***). Linear regression fit for purely repulsive hystereses was $R^2 = 0.84$. All FRs were measured in $CaCO_3$-saturated solutions within 25 h.*

Areas of hystereses between the force-distance curves on approach and on separation can provide additional information about changing sample topography. We observed two types of hystereses: adhesive hystereses for attractive FRs in CM; and hystereses fully located in the repulsive region of the force-distance curves for the repulsive FRs in CC and CM. We argue that these repulsive hystereses were mainly related to both mechanical effects during the loading-unloading cycles and to the changes in calcite thickness on dissolution and growth. The hystereses that would be produced by a mechanical backlash or thermal drifts would be significantly smaller than that the ones we observed.

The areas of hystereses between the FR on approach and on separation, normalized by the maximum applied load, were plotted in **Figure 13** as a function of the exponential decay length λ of the FRs on approach (~estimated roughness in the contact area). We found that these areas were proportional

to the roughness of the contacts established in the SFA: the larger the roughness magnitude, the larger the hystereses both in CC and CM. In some cases, the hystereses could be fully attributed to dissolution (due to changes in HP and calcite thickness; **Figure S20**). In many cases, however, the large areas of hystereses could not be accounted only to dissolution or growth (**Figures 10, S21, S22**). We also measured FRs with no hystereses for relatively smooth calcite surfaces in CC ($4<\lambda<9$ nm), reflecting a dominance of elastic compression in these cases (e.g. **Figure S22**, runs 4–10).

Hystereses in the force-distance curves in the SFA can arise due to adhesion forces, irreversible surface deformation (dissolution or plastic deformation), but also due to surface roughness. The adhesion hysteresis is related to a difference in the adhesion energy, which is larger on unloading (a contracting contact area) than on loading (a growing contact area) [25]. Hystereses related to the fast dissolution/growth occur because the sample thickness is changed during the loading-unloading cycles. Plastic deformation produces irreversible hystereses also because of the changes in a sample thickness but mostly because the energy needed to deform the surface plastically is not released back on unloading as in the case of a perfectly elastic smooth contact. Finally, hystereses in the repulsive region of the force-distance curves can be present for elastic contacts due to roughness of the surfaces [82, 105]. In such cases the number of asperities is higher on separation, and while some asperities still experience compression during the unloading, other shorter ones are stretched out and exert a tensile load on the opposing surface, decreasing the net load at a given separation. This behavior, however, has been evidenced in the case of adhesive interaction between rough surfaces [82, 105]. In our system, such mechanisms could possibly partially explain the repulsive hystereses in CM, when the pull-off forces were not measured due to high surface roughness. It is less likely that rough repulsive contacts (as in CC) between elastic surfaces would experience such interaction, as the small asperity junctions can be described as a set of Hertzian-like repulsive contacts without tensile stretching as predicted for JKR-type adhesive contacts. Although we assumed before that the loading of the asperities was dominantly an elastic process, such process should

not produce the sometimes observed large hystereses, especially at times when dissolution of surfaces was limited.

The previously calculated PI values suggested that plastic deformation was likely for our rough calcite films. The PI parameter implies that plastic deformation is easier for smaller asperities, and that deformation degree is higher when there are more asperities on the surface. This agrees with the trend observed in **Figure 13**, showing larger hystereses for the rougher surfaces having more asperities. In the experiments in which calcite films underwent significant recrystallization and roughening overnight (CM350A, **Figure 5**; CC350A, **Figure 6**), the observed hystereses seem to be clearly indicative of subsequent plastic deformation of the recrystallized layer (**Figure S21**, runs 9–14; **Figure S22**, runs 12–18): the areas of hystereses decreased in the consecutive FRs and the HP shifted to lower values, but the FR on separation did not show any progressing dissolution of the surfaces (as in **Figure S20** where the FR on retraction shifts to smaller D values despite moving the surfaces out). When the surfaces were more reactive, resulting in faster HP shifts, it was difficult to separate dissolution and the HP shifts due to deformation, as the dissolution rates were not constant and could be very easily misestimated. Similarly, we could not observe a major reduction of hystereses in the repeated loading-unloading cycles for more reactive surfaces (which should happen as the degree of irreversible deformation would be gradually smaller). Highly likely, the plastic deformation/pressure solution still occurred at the asperity tips in most cases, but the contact topography was affected by recrystallization in the same time, 'renewing' the contacts for deformation. Gradually reduced but not completely eliminated hystereses have been previously observed on repeated loading-unloading for plastically deforming asperities, which exhibited some recovery of deformation when the surfaces were separated [106]. We thus suggest that in our system, in the case of repulsive contacts with no pronounced growth or dissolution, λ of the FR during loading could be interpreted as due to both reversible and irreversible deformation of the asperities in the contact, and λ of the FR during unloading would be indicative of the magnitude of reversible compression.

It is also possible that when two rough surfaces were contacted, the asperities aligning in contact and separating from the established contact experienced friction. This could be reflected in FRs on approach where more energy would be needed to bring such rough surfaces into contacts, and in FRs on separation where friction would oppose the surface retraction, adding to hystereses. However, such contribution would not be present in CM, in which system one surface was atomically smooth.

Implications

The crucial role of interfacial fluids in deformation of porous carbonate sediments is manifested in much higher rates of chemical compaction than of mechanical compaction. The high reactivity and solubility of $CaCO_3$, relatively to silicate and aluminosilicate minerals, and high porosity of carbonate rocks makes them especially prone to phenomena such as the water-weakening [9]. In our system, we generally observed two processes with an opposite effect on the strengthening of solid-solid interfaces: 1) nm-scale recrystallization in water, leading to relatively strong repulsive effects between the surfaces; 2) increase in contact area, and thus the adhesion force between the surfaces.

Firstly, the experimentally observed lower mechanical strength of water-saturated carbonate rocks, such as chalk, at very short time scales, has been attributed to the loss of cohesion between the individual calcite grains in water [2]. This relatively fast loss of cohesion has been linked with various mechanical and chemical mechanisms [2, 11, 19, 23, 107-110]. However, the possible increase of calcite roughness upon equilibration with pore fluids of varied chemistry, even at a nm-scale, has rarely been discussed in relation to the water-weakening. We showed that the confined calcite surfaces can recrystallize and grow even when the bulk solution is undersaturated with respect to calcite. The mechanical effects related to nm-scale recrystallization of calcite surfaces could cause the observed repulsive force to be of much higher magnitude and onset than the EDL repulsive forces and even the strongly repulsive hydration forces. We thus propose that the nm-scale recrystallization of calcite surfaces at solid-solid contacts in water can additionally cause a significant decrease in cohesion between calcite grains. Assuming that the real contact area in our system was only a small fraction of the nominal contact area, the force of crystallization associated with the nm-scale recrystallization of calcite crystals could overcome the confining pressures of the order of MPa.

Secondly, we showed that the gradual pressure-driven deformation of calcite asperities in contact with mica was most likely responsible for the observed smoothening of contact areas and the increase in

pull-off forces, and thus the strengthening of the interface between these two minerals. Such phenomenon can have a major significance for an increased resistance of frictional interfaces [111].

Moreover, the observed increase of calcite roughness in water can be significant for EOR in chalk and many industrial systems, as apart from enhancing the repulsive forces between contacting calcite grains, it also affects the surface wettability properties [31].

Conclusions

We showed that the topographical evolution of rough calcite surfaces depended on the degree of confinement, with rougher contacts being less isolated from the bulk fluid, and undergoing more pronounced dissolution. Prolonged dissolution and limited mass transport between the smoothest sets of surfaces could lead to increasing supersaturation in the gap between the surfaces, calcite growth, major roughening, and the force of crystallization that could overcome confining pressures of the order of MPa. The changes in surface roughness were closely related to the forces acting between the surfaces. The rougher the surfaces, the higher the magnitude of the repulsive contact force, which was related to mechanical work needed to compress multiple asperities on loading. The repeated loading-unloading cycles in the case of adhesive systems led to a gradual increase in pull-off forces due to increasing contact areas, most likely caused by a progressive pressure-driven deformation of asperities on the rough calcite surfaces. Only repulsive forces between even the smoothest two calcite surfaces were measured, possibly related to repulsive hydration effects. The relatively strong adhesive interaction between smoother calcite and atomically smooth mica surfaces was likely enhanced by electrostatic effects. We propose that surface roughening of calcite in water could be another mechanism that enhances water-weakening effect in carbonates by decreasing cohesion between calcite grains and facilitating grain sliding upon compaction.

SUPPORTING INFORMATION

Supporting Information (SI) includes: details of SFA and Reflcalc analysis; detailed ALD parameters; forces in MM in $CaCO_3$-saturated solutions; equations used to model DLVO and roughness; boundary layer calculations; and supplementary results related to SFA force measurements and substrate reactivity.

ACKNOWLEDGEMENTS

This project has received funding from the European Union Horizon 2020 research and innovation program under the Marie Skłodowska-Curie grant agreement no. 642976-NanoHeal Project. This work reflects only the author's view and the Commission is not responsible for any use that may be made of the information it contains. SJ acknowledges the National IOR center of Norway under project no. PR-10373. The AFM measurements were perfomed by the JKR system funded by B. Jamtveit from the European Union's Horizon 2020 research and innovation programme under the ERC advanced Grant Agreement (669972). B. Løken Berg is acknowledged for the help with SEM. G. Jonski is acknowledged for the assistance with AAS. We thank L. de Ruiter and O. B. Karlsen for the useful advice and the anonymous reviewers for their valuable comments.

References

1. Han, R.; Shimamoto, T.; Hirose, T.; Ree, J.-H.; Ando, J.-i., Ultralow friction of carbonate faults caused by thermal decomposition. *Science* **2007,** *316* (5826), 878-881.
2. Risnes, R.; Madland, M.; Hole, M.; Kwabiah, N., Water weakening of chalk—Mechanical effects of water–glycol mixtures. *J. Pet. Sci. Eng.* **2005,** *48* (1), 21-36.
3. Eichmann, S. L.; Burnham, N. A., Calcium-Mediated Adhesion of Nanomaterials in Reservoir Fluids. *Scientific Reports* **2017,** *7*.
4. Liberto, T.; Le Merrer, M.; Barentin, C.; Bellotto, M.; Colombani, J., Elasticity and yielding of a calcite paste: scaling laws in a dense colloidal suspension. *Soft Matter* **2017,** *13* (10), 2014-2023.
5. Kovačević, V.; Lučić, S.; Cerovečki, Ž., Influence of filler surface pre-treatment on the mechanical properties of composites. *Int. J. Adhes. Adhes.* **1997,** *17* (3), 239-245.
6. Benachour, Y.; Davy, C. A.; Skoczylas, F.; Houari, H., Effect of a high calcite filler addition upon microstructural, mechanical, shrinkage and transport properties of a mortar. *Cem. Concr. Res.* **2008,** *38* (6), 727-736.
7. Carretero, M. I.; Pozo, M., Clay and non-clay minerals in the pharmaceutical industry: Part I. Excipients and medical applications. *Appl. Clay Sci.* **2009,** *46* (1), 73-80.
8. Brantut, N.; Heap, M.; Meredith, P.; Baud, P., Time-dependent cracking and brittle creep in crustal rocks: A review. *J. Struct. Geol.* **2013,** *52*, 17-43.
9. Wong, L.; Maruvanchery, V., Water effects on rocks. *Rock Mechanics and Rock Engineering: From the Past to the Future* **2016**, 187.
10. Teufel, L. W.; Rhett, D. W.; Farrell, H. E., Effect of reservoir depletion and pore pressure drawdown on in situ stress and deformation in the Ekofisk field, North Sea. *The 32nd US Symposium on Rock Mechanics (USRMS), American Rock Mechanics Association*, **1991**.
11. Newman, G. H., The effect of water chemistry on the laboratory compression and permeability characteristics of some North Sea chalks. *J. Pet. Technol.* **1983,** *35* (05), 976-980.
12. Hellmann, R.; Renders, P. J.; Gratier, J.-P.; Guiguet, R., Experimental pressure solution compaction of chalk in aqueous solutions. Part 1. Deformation behavior and chemistry. *Water-rock interactions, ore deposits, and environmental geochemistry: A tribute to David A. Crerar* **2002,** *7*, 129-152.
13. Zhang, X.; Spiers, C. J.; Peach, C. J., Compaction creep of wet granular calcite by pressure solution at 28 C to 150 C. *J. Geophys. Res.: Solid Earth* **2010,** *115* (B9).
14. Liteanu, E.; Spiers, C.; De Bresser, J., The influence of water and supercritical CO 2 on the failure behavior of chalk. *Tectonophysics* **2013,** *599*, 157-169.
15. Croizé, D.; Renard, F.; Bjørlykke, K.; Dysthe, D. K., Experimental calcite dissolution under stress: Evolution of grain contact microstructure during pressure solution creep. *J. Geophys. Res.: Solid Earth* **2010,** *115* (B9).
16. Croize, D.; Renard, F.; Gratier, J.-P., Compaction and porosity reduction in carbonates: A review of observations, theory, and experiments. *Adv. Geophys.* **2013,** *54*, 181-238.
17. Risnes, R., Deformation and yield in high porosity outcrop chalk. *Phys. Chem. Earth, Part A.* **2001,** *26* (1-2), 53-57.
18. Dunning, J.; Douglas, B.; Miller, M.; McDonald, S., The role of the chemical environment in frictional deformation: stress corrosion cracking and comminution. *Pure Appl. Geophys.* **1994,** *143* (1), 151-178.
19. Røyne, A.; Bisschop, J.; Dysthe, D. K., Experimental investigation of surface energy and subcritical crack growth in calcite. *J. Geophys. Res.: Solid Earth* **2011,** *116* (B4).
20. Megawati, M.; Hiorth, A.; Madland, M., The impact of surface charge on the mechanical behavior of high-porosity chalk. *Rock mechanics and rock engineering* **2013,** *46* (5), 1073-1090.

21. Levenson, Y.; Emmanuel, S., Repulsion between calcite crystals and grain detachment during water–rock interaction. *Geochem. Perspect. Lett.* **2017,** *3*, 133-141.
22. Brekke-Svaland, G.; Bresme, F., Interactions Between Hydrated Calcium Carbonate Surfaces at Nanoconfinement Conditions. *J. Phys. Chem. C* **2018**.
23. Røyne, A.; Dalby, K. N.; Hassenkam, T., Repulsive hydration forces between calcite surfaces and their effect on the brittle strength of calcite-bearing rocks. *Geophys. Res. Lett.* **2015,** *42* (12), 4786-4794.
24. Diao, Y.; Espinosa-Marzal, R. M., Molecular insight into the nanoconfined calcite–solution interface. *Proc. Natl. Acad. Sci. U.S.A.* **2016,** *113* (43), 12047-12052.
25. Israelachvili, J. N., *Intermolecular and surface forces*. Academic press: 2015.
26. Stipp, S., Toward a conceptual model of the calcite surface: hydration, hydrolysis, and surface potential. *Geochim. Cosmochim. Acta* **1999,** *63* (19), 3121-3131.
27. Geissbühler, P.; Fenter, P.; DiMasi, E.; Srajer, G.; Sorensen, L.; Sturchio, N., Three-dimensional structure of the calcite–water interface by surface X-ray scattering. *Surf. Sci.* **2004,** *573* (2), 191-203.
28. Fenter, P.; Kerisit, S.; Raiteri, P.; Gale, J. D., Is the calcite–water interface understood? Direct comparisons of molecular dynamics simulations with specular X-ray reflectivity data. *J. Phys. Chem. C* **2013,** *117* (10), 5028-5042.
29. Bohr, J.; Wogelius, R. A.; Morris, P. M.; Stipp, S. L., Thickness and structure of the water film deposited from vapour on calcite surfaces. *Geochim. Cosmochim. Acta* **2010,** *74* (21), 5985-5999.
30. Ulusoy, U.; Yekeler, M., Correlation of the surface roughness of some industrial minerals with their wettability parameters. *Chem. Eng. Process.* **2005,** *44* (5), 555-563.
31. Chen, S.-Y.; Kaufman, Y.; Kristiansen, K.; Seo, D.; Schrader, A. M.; Alotaibi, M. B.; Dobbs, H. A.; Cadirov, N. A.; Boles, J. R.; Ayirala, S. C., Effects of salinity on oil recovery (the 'dilution effect'): Experimental and theoretical studies of crude oil/brine/carbonate surface restructuring and associated physico-chemical interactions. *Energy Fuels* **2017**.
32. Valtiner, M.; Banquy, X.; Kristiansen, K.; Greene, G. W.; Israelachvili, J. N., The electrochemical surface forces apparatus: The effect of surface roughness, electrostatic surface potentials, and anodic oxide growth on interaction forces, and friction between dissimilar surfaces in aqueous solutions. *Langmuir* **2012,** *28* (36), 13080-13093.
33. Eom, N.; Parsons, D. F.; Craig, V. S., Roughness in Surface Force Measurements: Extension of DLVO Theory to Describe the Forces Between Hafnia Surfaces. *J. Phys. Chem. B* **2017**.
34. Parsons, D. F.; Walsh, R. B.; Craig, V. S., Surface forces: Surface roughness in theory and experiment. *J. Chem. Phys.* **2014,** *140* (16), 164701.
35. Wolthers, M.; Di Tommaso, D.; Du, Z.; de Leeuw, N., Calcite surface structure and reactivity: molecular dynamics simulations and macroscopic surface modelling of the calcite–water interface. *Phys. Chem. Chem. Phys.* **2012,** *14* (43), 15145-15157.
36. Stipp, S.; Eggleston, C.; Nielsen, B., Calcite surface structure observed at microtopographic and molecular scales with atomic force microscopy (AFM). *Geochim. Cosmochim. Acta* **1994,** *58* (14), 3023-3033.
37. Heuberger, M.; Luengo, G.; Israelachvili, J., Topographic information from multiple beam interferometry in the surface forces apparatus. *Langmuir* **1997,** *13* (14), 3839-3848.
38. Merola, C.; Cheng, H.-W.; Schwenzfeier, K.; Kristiansen, K.; Chen, Y.-J.; Dobbs, H.; Israelachvili, J.; Valtiner, M., In situ nano-to microscopic imaging and growth mechanism of electrochemical dissolution (eg, corrosion) of a confined metal surface. *Proc. Natl. Acad. Sci. U.S.A.* **2017,** *114* (36), 9541-9546.
39. Horn, R.; Clarke, D.; Clarkson, M., Direct measurement of surface forces between sapphire crystals in aqueous solutions. *J. Mater. Res.* **1988,** *3* (03), 413-416.
40. Horn, R.; Smith, D.; Haller, W., Surface forces and viscosity of water measured between silica sheets. *Chem. Phys. Lett.* **1989,** *162* (4-5), 404-408.

41. Hirz, S.; Homola, A.; Hadziioannou, G.; Frank, C., Effect of substrate on shearing properties of ultrathin polymer films. *Langmuir* **1992,** *8* (1), 328-333.
42. Steinberg, S.; Ducker, W.; Vigil, G.; Hyukjin, C.; Frank, C.; Tseng, M.; Clarke, D.; Israelachvili, J., Van der Waals Epitaxial Growth of -Alumina Nanocrystals on Mica. *Science* **1993,** *260*, 656-656.
43. Teng, F.; Zeng, H.; Liu, Q., Understanding the deposition and surface interactions of gypsum. *J. Phys. Chem. C* **2011,** *115* (35), 17485-17494.
44. Nilsen, O.; Fjellvag, H.; Kjekshus, A., Growth of calcium carbonate by the atomic layer chemical vapour deposition technique. *Thin Solid Films* **2004,** *450* (2), 240-247.
45. Reithmeier, M.; Erbe, A., Dielectric interlayers for increasing the transparency of metal films for mid-infrared attenuated total reflection spectroscopy. *Phys. Chem. Chem. Phys.* **2010,** *12* (44), 14798-14803.
46. Israelachvili, J. N.; Alcantar, N. A.; Maeda, N.; Mates, T. E.; Ruths, M., Preparing contamination-free mica substrates for surface characterization, force measurements, and imaging. *Langmuir* **2004,** *20* (9), 3616-3622.
47. Israelachvili, J.; Min, Y.; Akbulut, M.; Alig, A.; Carver, G.; Greene, W.; Kristiansen, K.; Meyer, E.; Pesika, N.; Rosenberg, K.; Zeng, H., Recent advances in the surface forces apparatus (SFA) technique. *Rep. Prog. Phys.* **2010,** *73* (3).
48. Israelachvili, J., Thin film studies using multiple-beam interferometry. *J. Colloid Interface Sci.* **1973,** *44* (2), 259-272.
49. Israelachvili, J. N.; Adams, G. E., Measurement of forces between two mica surfaces in aqueous electrolyte solutions in the range 0–100 nm. *J. Chem. Soc., Faraday Trans. 1* **1978,** *74*, 975-1001.
50. Israelachvili, J. N.; McGuiggan, P. M., Adhesion and short-range forces between surfaces. Part I: New apparatus for surface force measurements. *J. Mater. Res.* **1990,** *5* (10), 2223-2231.
51. Tolansky, S., Multiple-beam interferometry of surfaces and films. *Dover Publications,* **1970**.
52. Derjaguin, B., Untersuchungen über die Reibung und Adhäsion, IV. *Kolloid-Zeitschrift* **1934,** *69* (2), 155-164.
53. Schubert, M., Polarization-dependent optical parameters of arbitrarily anisotropic homogeneous layered systems. *Phys. Rev. B* **1996,** *53* (8), 4265.
54. Cloots, R., Raman spectrum of carbonates MIICO3 in the 1100-1000cm^{-1} region: observation of the v1, mode of the isotopic (C16O182O) 2− ion. *Spectrochim. Acta, Part A* **1991,** *47* (12), 1745-1750.
55. Gillet, P.; Biellmann, C.; Reynard, B.; McMillan, P., Raman spectroscopic studies of carbonates Part I: High-pressure and high-temperature behaviour of calcite, magnesite, dolomite and aragonite. *Phys. Chem. Miner.* **1993,** *20* (1), 1-18.
56. Kontoyannis, C. G.; Vagenas, N. V., Calcium carbonate phase analysis using XRD and FT-Raman spectroscopy. *Analyst* **2000,** *125* (2), 251-255.
57. Porto, S.; Giordmaine, J.; Damen, T., Depolarization of Raman scattering in calcite. *Phys. Rev.* **1966,** *147* (2), 608.
58. Buzgar, N.; Apopei, A. I., The Raman study of certain carbonates. *Analele Stiintifice de Universitatii AI Cuza din Iasi. Sect. 2, Geologie* **2009,** *55* (2), 97.
59. Wehrmeister, U.; Soldati, A.; Jacob, D.; Häger, T.; Hofmeister, W., Raman spectroscopy of synthetic, geological and biological vaterite: a Raman spectroscopic study. *J. Raman Spectrosc.* **2010,** *41* (2), 193-201.
60. Wehrmeister, U.; Jacob, D.; Soldati, A.; Loges, N.; Häger, T.; Hofmeister, W., Amorphous, nanocrystalline and crystalline calcium carbonates in biological materials. *J. Raman Spectrosc.* **2011,** *42* (5), 926-935.
61. Skinner, L.; Sambles, J., The Kelvin equation—a review. *J. Aerosol Sci.* **1972,** *3* (3), 199-210.
62. Greenwood, G., The growth of dispersed precipitates in solutions. *Acta Metall.* **1956,** *4* (3), 243-248.

63. Renard, F.; Røyne, A.; Putnis, C. V., Timescales of interface-coupled dissolution-precipitation reactions on carbonates. *Geosci. Front.* **2018**.
64. Putignano, C.; Afferrante, L.; Carbone, G.; Demelio, G. P., A multiscale analysis of elastic contacts and percolation threshold for numerically generated and real rough surfaces. *Tribol. Int.* **2013,** *64*, 148-154.
65. Gibbs, J. W., On the Equilibrium of Heterogeneous Substances. *Am. J. Sci. Arts (1820-1879)* **1878,** *16* (96), 441.
66. Rutter, E.; Elliott, D., The kinetics of rock deformation by pressure solution. *Philos. Trans. Royal Soc. A* **1976**, 203-219.
67. Persson, B. N., Contact mechanics for randomly rough surfaces. *Surf. Sci. Rep.* **2006,** *61* (4), 201-227.
68. Turner, F. J.; T GRIGGS, D.; Heard, H., Experimental deformation of calcite crystals. *Geol. Soc. Am. Bull.* **1954,** *65* (9), 883-934.
69. Anzalone, A.; Boles, J.; Greene, G.; Young, K.; Israelachvili, J.; Alcantar, N., Confined fluids and their role in pressure solution. *Chem. Geol.* **2006,** *230* (3-4), 220-231.
70. Alcantar, N.; Israelachvili, J.; Boles, J., Forces and ionic transport between mica surfaces: Implications for pressure solution. *Geochim. Cosmochim. Acta* **2003,** *67* (7), 1289-1304.
71. Hickman, S. H.; Evans, B., Experimental pressure solution in halite: the effect of grain/interphase boundary structure. *Journal of the Geological Society* **1991,** *148* (3), 549-560.
72. Weyl, P. K., Pressure solution and the force of crystallization: a phenomenological theory. *J. Geophys. Res.* **1959,** *64* (11), 2001-2025.
73. Kristiansen, K.; Valtiner, M.; Greene, G. W.; Boles, J. R.; Israelachvili, J. N., Pressure solution–The importance of the electrochemical surface potentials. *Geochim. Cosmochim. Acta* **2011,** *75* (22), 6882-6892.
74. Greene, G. W.; Kristiansen, K.; Meyer, E. E.; Boles, J. R.; Israelachvili, J. N., Role of electrochemical reactions in pressure solution. *Geochim. Cosmochim. Acta* **2009,** *73* (10), 2862-2874.
75. Wolthers, M.; Charlet, L.; Van Cappellen, P., The surface chemistry of divalent metal carbonate minerals; a critical assessment of surface charge and potential data using the charge distribution multi-site ion complexation model. *Am. J. Sci.* **2008,** *308* (8), 905-941.
76. Dove, P. M.; Hochella, M. F., Calcite precipitation mechanisms and inhibition by orthophosphate: In situ observations by Scanning Force Microscopy. *Geochim. Cosmochim. Acta* **1993,** *57* (3), 705-714.
77. Bergström, L., Hamaker constants of inorganic materials. *Adv. Colloid Interface Sci.* **1997,** *70*, 125-169.
78. Oosawa, F., Polyelectrolytes. In *Polyelectrolytes*, Marcel Dekker: 1971.
79. Wennerström, H.; Jönsson, B.; Linse, P., The cell model for polyelectrolyte systems. Exact statistical mechanical relations, Monte Carlo simulations, and the Poisson–Boltzmann approximation. *J. Chem. Phys.* **1982,** *76* (9), 4665-4670.
80. Kjellander, R.; Marcelja, S.; Pashley, R.; Quirk, J., Double-layer ion correlation forces restrict calcium-clay swelling. *J. Phys. Chem.* **1988,** *92* (23), 6489-6492.
81. Benz, M.; Rosenberg, K. J.; Kramer, E. J.; Israelachvili, J. N., The deformation and adhesion of randomly rough and patterned surfaces. *J. Phys. Chem. B* **2006,** *110* (24), 11884-11893.
82. Zappone, B.; Rosenberg, K. J.; Israelachvili, J., Role of nanometer roughness on the adhesion and friction of a rough polymer surface and a molecularly smooth mica surface. *Tribol. Lett.* **2007,** *26* (3), 191.
83. Fuller, K.; Tabor, D., The effect of surface roughness on the adhesion of elastic solids. *Proc. R. Soc. London, Ser. A* **1975**, pp 327-342.
84. Peressadko, A.; Hosoda, N.; Persson, B., Influence of surface roughness on adhesion between elastic bodies. *Phys. Rev. Lett.* **2005,** *95* (12), 124301.

85. Archard, J., Elastic deformation and the laws of friction. *Proc. R. Soc. London, Ser. A* **1957**, pp 190-205.
86. Persson, B.; Bucher, F.; Chiaia, B., Elastic contact between randomly rough surfaces: comparison of theory with numerical results. *Phys. Rev. B* **2002,** *65* (18), 184106.
87. Bush, A.; Gibson, R.; Thomas, T., The elastic contact of a rough surface. *Wear* **1975,** *35* (1), 87-111.
88. Greenwood, J.; Williamson, J. P., Contact of nominally flat surfaces. *Proc. R. Soc. Lond. Ser. A* **1966**, pp 300-319.
89. Whitney, D. L.; Fayon, A. K.; Broz, M. E.; Cook, R. F., Exploring the Relationship of Scratch Resistance, Hardness, and other Physical Properties of Minerals using Mohs Scale Minerals. *Journal of Geoscience Education* **2007,** *55* (1), 56-61.
90. Røyne, A.; Dysthe, D. K., Rim formation on crystal faces growing in confinement. *J. Cryst. Growth* **2012,** *346* (1), 89-100.
91. Paterson, M., Nonhydrostatic thermodynamics and its geologic applications. *Rev. Geophys.* **1973,** *11* (2), 355-389.
92. Hillner, P.; Gratz, A.; Manne, S.; Hansma, P., Atomic-scale imaging of calcite growth and dissolution in real time. *Geology* **1992,** *20* (4), 359-362.
93. Bisschop, J.; Dysthe, D.; Putnis, C.; Jamtveit, B., In situ AFM study of the dissolution and recrystallization behaviour of polished and stressed calcite surfaces. *Geochim. Cosmochim. Acta* **2006,** *70* (7), 1728-1738.
94. Dysthe, D. K.; Wogelius, R. A.; Tang, C.; Nield, A., Evolution of mineral–fluid interfaces studied at pressure with synchrotron X-ray techniques. *Chem. Geol.* **2006,** *230* (3), 232-241.
95. Chiarello, R. P.; Wogelius, R. A.; Sturchio, N. C., In-situ synchrotron X-ray reflectivity measurements at the calcite-water interface. *Geochim. Cosmochim. Acta* **1993,** *57* (16), 4103-4110.
96. Scherer, G. W., Crystallization in pores. *Cement Concrete Res.* **1999,** *29* (8), 1347-1358.
97. Jones, R.; Pollock, H. M.; Cleaver, J. A.; Hodges, C. S., Adhesion forces between glass and silicon surfaces in air studied by AFM: Effects of relative humidity, particle size, roughness, and surface treatment. *Langmuir* **2002,** *18* (21), 8045-8055.
98. Rabinovich, Y. I.; Adler, J. J.; Ata, A.; Singh, R. K.; Moudgil, B. M., Adhesion between nanoscale rough surfaces: II. Measurement and comparison with theory. *J. Colloid Interf. Sci.* **2000,** *232* (1), 17-24.
99. Katainen, J.; Paajanen, M.; Ahtola, E.; Pore, V.; Lahtinen, J., Adhesion as an interplay between particle size and surface roughness. *J. Colloid Interf. Sci.* **2006,** *304* (2), 524-529.
100. Levins, J. M.; Vanderlick, T. K., Impact of roughness on the deformation and adhesion of a rough metal and smooth mica in contact. *J. Phys. Chem.* **1995,** *99* (14), 5067-5076.
101. Beach, E.; Tormoen, G.; Drelich, J.; Han, R., Pull-off force measurements between rough surfaces by atomic force microscopy. *J. Colloid Interf. Sci.* **2002,** *247* (1), 84-99.
102. Donaldson Jr, S. H.; Røyne, A.; Kristiansen, K.; Rapp, M. V.; Das, S.; Gebbie, M. A.; Lee, D. W.; Stock, P.; Valtiner, M.; Israelachvili, J., Developing a general interaction potential for hydrophobic and hydrophilic interactions. *Langmuir* **2014,** *31* (7), 2051-2064.
103. Pashley, R. M., Hydration Forces between Mica Surfaces in Aqueous-Electrolyte Solutions. *J. Colloid Interf. Sci.* **1981,** *80* (1), 153-162.
104. Pashley, R.; Israelachvili, J., DLVO and hydration forces between mica surfaces in Mg2+, Ca2+, Sr2+, and Ba2+ chloride solutions. *J. Colloid Interf. Sci.* **1984,** *97* (2), 446-455.
105. Kesari, H.; Doll, J. C.; Pruitt, B. L.; Cai, W.; Lew, A. J., Role of surface roughness in hysteresis during adhesive elastic contact. *Philos. Mag.* **2010,** *90* (12), 891-902.
106. Quon, R.; Knarr, R.; Vanderlick, T., Measurement of the deformation and adhesion of rough solids in contact. *J. Phys. Chem. B* **1999,** *103* (25), 5320-5327.
107. Delage, P.; Schroeder, C.; Cui, Y. J., Subsidence and capillary effects in chalks. *arXiv preprint arXiv:0803.1308* **2008**.

108. Korsnes, R. I.; Madland, M. V.; Austad, T.; Haver, S.; Røsland, G., The effects of temperature on the water weakening of chalk by seawater. *J. Pet. Sci. Eng.* **2008,** *60* (3-4), 183-193.
109. Madland, M. V.; Korsnes, R. I.; Risnes, R., Temperature effects in Brazilian, uniaxial and triaxial compressive tests with high porosity chalk. *SPE Annual Technical Conference and Exhibition, Society of Petroleum Engineers,* **2002.**
110. Nermoen, A.; Korsnes, R. I.; Hiorth, A.; Madland, M. V., Porosity and permeability development in compacting chalks during flooding of nonequilibrium brines: Insights from long-term experiment. *J. Geophys. Res.: Solid Earth* **2015,** *120* (5), 2935-2960.
111. Renard, F.; Beauprêtre, S.; Voisin, C.; Zigone, D.; Candela, T.; Dysthe, D. K.; Gratier, J.-P., Strength evolution of a reactive frictional interface is controlled by the dynamics of contacts and chemical effects. *Earth Planet. Sci. Lett.* **2012,** *341*, 20-34.

TABLE OF CONTENTS GRAPHIC